Flow Turbulence Combust (2011) 87:673–705
DOI 10.1007/s10494-011-9351-2

DNS of Fractal-Generated Turbulence

Sylvain Laizet · John Christos Vassilicos

Received: 4 January 2011 / Accepted: 4 May 2011 / Published online: 29 May 2011

Abstract An innovative approach which combines high order compact schemes, Immersed Boundary Method and an efficient domain decomposition method is used to perform high fidelity Direct Numerical Simulations (DNS) of four spatially evolving turbulent flows, one generated by a regular grid and three generated by fractal square grids. The main results which we have been able to obtain from these simulations are the following: the vorticity field appears more clustered when generated by fractal square grids compared to a regular grid; fractal square grids generate higher vorticities and turbulence intensities than a regular grid; the flow holds clear geometrical imprints of the fractal grids far downstream, a property which could be used in the future for flow design, management and passive control; the DNS obtained with fractal grids confirmed the existence of two turbulent regions, one where the turbulence progressively amplifies closer to the grid (the production region) followed by one where the turbulence decays; the energy spectra of fluctuating turbulent velocities at various locations in the production region of the flow provide some information on how the turbulence is generated at the smallest scales first near the grid where the smallest wakes are dominant, followed by progressively smaller turbulent frequencies further downstream where progressively larger wakes interact.

Keywords Turbulence · Direct numerical simulation · Immersed boundary method · Vortex dynamics

S. Laizet (✉) · J. C. Vassilicos
Department of Aeronautics, Imperial College London, South Kensington Campus,
London SW7 2AZ, UK
e-mail: s.laizet@imperial.ac.uk

J. C. Vassilicos
e-mail: j.c.vassiliocs@imperial.ac.uk

1 Introduction

Homogeneous isotropic turbulence has been widely studied both experimentally in wind or water tunnels and numerically by Direct Numerical Simulations (DNS) carried out with spectral methods in periodic boxes (e.g. the DNS with $4,096^3$ of [5]. Recently, Hurst and Vassilicos [4] and Mazellier and Vassilicos [14] used various multiscale (fractal) grids to generate turbulence in wind tunnels and found that complex multiscale boundary/initial conditions can drastically influence the behaviour of a turbulent flow, especially when a fractal square grid (see Figs. 1 and 3) is placed at the entry of a wind tunnel test section. For example, it is possible to tune the shape and various parameters defining a fractal grid (see definitions in Section 2.2) so as to design a very efficient static inline mixer with small pressure drop for low power losses and thinner walls but also high turbulent intensities at a desired location for good mixing within constrained space allocation [3].

Although the wind tunnel anemometry measurements have provided invaluable time-resolved information on the unique properties of multiscale-generated turbulent flows, it remains essential to investigate the full three-dimensional structure of the turbulence in order to better understand its underlying physics. Chester et al. [2] performed calculations of drag on fractal-like trees using Renormalized Numerical Simulation (RNS) to model the drag of the unresolved branches of the fractal tree. However, their approach did not allow them to investigate the actual turbulent flow structure. Very recently, Nagata et al. [17, 18] performed DNS of full three-dimensional turbulent flows generated by three different fractal grids but at relatively small Reynolds numbers. They have been able to recover some of the experimental results of [4, 14, 22], such as the higher turbulent intensities that fractal square grids generate by comparison to regular grids of same or even larger blockage ratio. Several simulations of multiscale-generated flows have already been performed by [7, 9]. In these simulations the fractal stirrers were mainly based on a square pattern with three multiscale iterations and with a relatively small computational domain in the streamwise direction. There were also successfully performed DNS of turbulence generated by a fractal cross grid at different spatial resolutions in order to validate the numerical strategy [10, 11]. These authors are using an innovative numerical tool, called **Incompact3d**, for DNS of multiscale-generated turbulent flows which

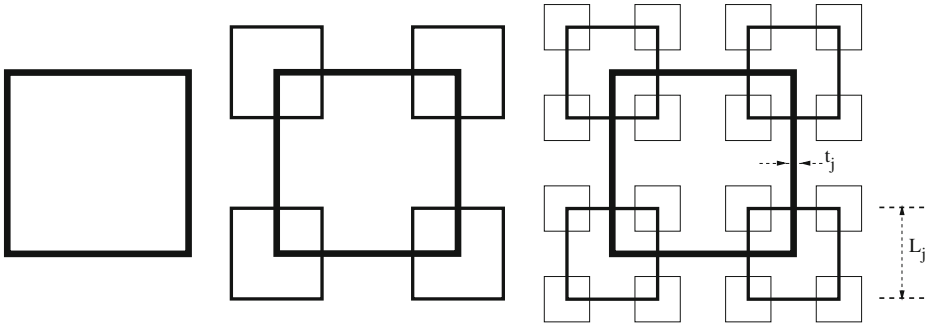

Fig. 1 Construction of a planal fractal square grid based on three fractal iterations

combines an Immersed Boundary Method (IBM) for the modelling of the grids with high-order schemes for the spatial discretisation on a Cartesian mesh [6]. In order to make the best use of the impressive advances in parallel platform architectures, Laizet et al. [7] successfully adapted a 1D domain decomposition, compatible with high-order compact schemes and the IBM used in the code.

Even if these preliminary results are very encouraging , there is a clear need for bigger simulations with a longer computational domain in the streamwise direction that can be undertaken with a decent wall clock time. Very recently, Laizet and Li [8] developed a new version of **Incompact3d** which is based on a 2D domain decomposition. It was shown [8] that this strategy can lead to excellent parallel efficiency with up to 262,000 computational cores, as seen in Fig. 2.

Note that with the old version of the code, the simulations presented in this paper would have taken several months in order to get well converged statistics. With the new version of the code only few days were required on the state-of-the-art supercomputer HECToR in the UK (www.hector.ac.uk), in order to obtain the results presented in this numerical study.

In this paper, we use the new version of **Incompact3d** [8] to compare different turbulent flows generated by three fractal square grids with different aspect ratios and one regular grid. The organisation of the paper is as follows. In Section 2, we present the main features of our DNS methodology, a brief description of the grids and the numerical parameters of each simulation. Some suggestive flow visualisations are presented and discussed in Section 3. Then, in order to better understand the

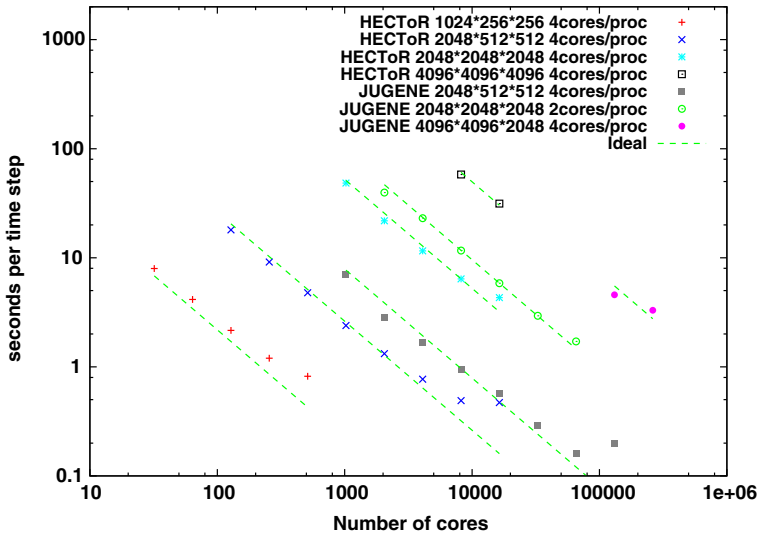

Fig. 2 Efficiency of the code on HECToR and on JUGENE. HECToR is a CRAY XT4 system based on quad-core processors, with a total of 22,656 computational cores. The theoretical peak performance of this system is 208 *Tflops*. JUGENE is a IBM Blue Gene/ based on quad-core processors, with a total of 294,912 computational cores. The theoretical peak performance of the system is 1 *Pflops*

underlying properties of each flow, some statistical results are presented in Section 4, followed by a conclusion in Section 5.

2 Flow parameters and numerical modelling

2.1 Numerical methods

To solve the incompressible Navier-Stokes equations, we use the in-house numerical code **Incompact3d** which is based on sixth-order compact schemes for spatial discretisation and a third-order Adams–Bashforth scheme for time advancement. To treat the incompressibility condition, a fractional step method requires to solve a Poisson equation. The main originality of this code is that this equation is fully solved in spectral space via the use of relevant 3D Fast Fourier transforms (FFT) which allows different sets of boundary conditions in each spatial direction: free-slip, periodic, inflow/outflow or Dirichlet boundary conditions on the velocity field. With the help of the concept of modified wavenumber introduced by [12], the divergence free condition is ensured up to machine accuracy.

The modelling of the grids is performed by an Immersed Boundary Method (IBM). Following the procedure proposed by [20], the present IBM is a direct forcing approach that ensures the no-slip boundary condition at the wall of the grid. The idea is to force the velocity to zero at the wall of the grids, as our particular Cartesian mesh does conform with the geometries of the grids. Combined with a sixth-order compact filtering of the convective terms, this specific IBM leads to a reduction of wiggles in the neighbourhood of the grid while allowing better quantitative predictions at marginal resolutions. A priori, the combination of a high-order scheme with the IBM can be problematic because of the discontinuity in velocity derivatives locally imposed by the artificial forcing term. However, even though the formal order of the solution is reduced as a result, the code has been demonstrated to be far more accurate with a 6th order scheme than with a 2nd order scheme both in statistics and instantaneous field realisations (see [19, 20] for more details). Furthermore, the Cartesian mesh does conform with the geometries of the fractal and regular grids of Fig. 3 because they consist of right angles and they are placed normal to the mean flow. Note finally that the pressure mesh is staggered from the velocity one by half a mesh to avoid spurious pressure oscillations introduced by the IBM. More details about the present code and its validation, especially the original treatment of the pressure in spectral space, can be found in [6].

DNS being the simplest approach conceptually to investigate turbulence, featuring the highest temporal and spatial accuracy with no modelling, it requires extraordinary powerful resources. For this numerical work, the version of **Incompact3d** based on a 2D domain decomposition has been used [8]. The code's 2D domain decomposition strategy offers three major advantages: the accuracy of the order of its sixth-order schemes has been maintained, it is fully compatible with the fully spectral solver for the Poisson equation and scalability is excellent up to hundreds of thousands computational cores, because, even though compact schemes are implicit in space, there is no data communication (overlapping) at the boundaries of each subdomain. More details about this 2D domain decomposition and its performance can be found in [8].

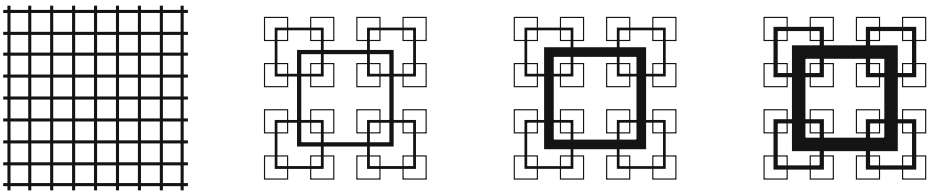

Fig. 3 Scaled diagrams of the four different grids used in this numerical study. From *left to right*: regular grid, fractal square grids with an aspect ratio of $t_r = 5,\ 6.5$ and 8.5. t_r is the ratio between the biggest and smallest lateral thicknesses on the fractal grids. Note that the lateral thickness of the smallest pattern is the same for all three fractal grids

2.2 Description of the grids

We use DNS to calculate the turbulent flows generated by one regular grid and three different fractal square grids. The three different fractal grids consist of different sized squares placed in a fractal-square-like pattern (see Fig. 3). These fractal grids are completely characterised by

- the number of fractal iterations, here $N = 3$;
- the number 4^j of square patterns at iteration j ($j = 0, 1, 2$ for $N = 3$);
- the lengths $L_j = R_L^j L_0$ and lateral thicknesses $t_j = R_t^j t_0$ (in the plane of the grid, normal to the mean flow) of the bars making the squares at iteration j. Here, $R_L = 1/2,\ L_0 = 0.5 L_y$ for all three grids, where L_y and L_z (with $L_y = L_z$) are the lateral sizes of the computational domain (see Fig. 4). Note that L_y and L_z are effectively equivalent to the lateral size T of the wind tunnel's square test section in the experimental measurements, though $L_0 + L_1 + L_2$ is a bit smaller than L_y in the present DNS. The three turbulence-generating grids differ by their values of R_t: $R_t = 0.447,\ 0.392,\ 0.343$ respectively. By definition, $L_0 = L_{\max}$, $L_{N-1} = L_{\min}$, $t_0 = t_{\max}$ and $t_{N-1} = t_{\min}$;

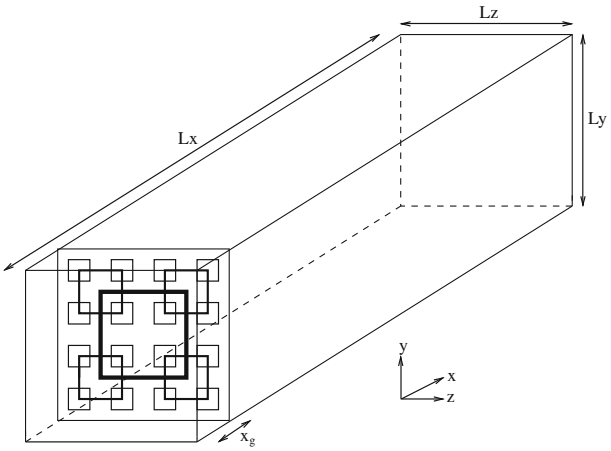

Fig. 4 Schematic view of the flow configuration for the fractal square grid

– the thickness ratio $t_r \equiv t_{\max}/t_{\min}$, i.e. the ratio between the lateral thickness of the bars making the largest square and the lateral thickness of the smallest. Note that, in the present work, $t_{\min}$ is set to the same value for all three fractal grids but that $t_r = 5,\ 6.5$ and 8.5 for the $R_t = 0.447,\ 0.392,\ 0.343$ grids respectively. Numerically, we set $t_{\min} = 1$ and $L_x = 460.8 t_{\min}$ where L_x is the longitudinal size of the computational domain (see Fig. 4).

The blockage ratios σ of our fractal grids, defined as the ratio of their total area in the lateral plane to the area $T^2 = L_y \times L_z$, are determined by our choices of these parameters and turn out to be ≈23% for the $t_r = 5$ grid, ≈27% for the $t_r = 6.5$ grid and ≈32% for the $t_r = 8.5$ grid.

Unlike regular grids, multiscale/fractal grids, and in particular the fractal square grids considered here, do not have a well-defined mesh size. This is why [4] introduced an effective mesh size for multiscale grids, $M_{\text{eff}} = \frac{4T^2}{P}\sqrt{1-\sigma}$ where P is the perimeter length in the $(y-z)$ plane of the zero-thickness fractal grid, i.e. where all thicknesses t_j have been artificially set to zero for the calculation of P. The multiscale nature of multiscale/fractal grids influences M_{eff} via the perimeter P which can be extremely long in spite of being constrained to fit within the area $T^2 = L_y \times L_z$. However, this definition of M_{eff} also returns the regular mesh size M, when applied to regular grids.

The effective mesh size is fully determined by our choices of parameters characterising the fractal grids and it turns out that $M_{\text{eff}} = (43.5/3)t_{\min}$ for the $t_r = 5$ grid, $(42/3)t_{\min}$ for the $t_r = 6.5$ grid and $(40/3)t_{\min}$ for the $t_r = 8.5$ grid. The regular grid considered here has the same blockage ratio as the $t_r = 8.5$ fractal grid and its mesh size M is equal to the effective mesh size of the $t_r = 8.5$ fractal grid. The lateral thickness of the bars making the regular grid is uniquely determined by σ and M. In terms of minimum lateral thickness $t_{\min}$ of the fractal grids it is $2.6t_{\min}$.

Note finally that the streamwise thickness of the bars is $2.4t_{\min}$ for all four grids, fractal and regular. In this numerical study, the only difference between each fractal grid is their thickness ratio.

2.3 Numerical parameters

The computational domain is $L_x \times L_y \times L_z = 460.8t_{\min} \times 115.2t_{\min} \times 115.2t_{\min}$ discretized on a Cartesian mesh of $n_x \times n_y \times n_z = 2305 \times 576 \times 576$ mesh nodes. It is split in 3,456 computational cores. For each grid, the simulation is performed with a Reynolds number $Re_{t_{\min}} = 300$ (based on the smallest lateral thickness $t_{\min}$ of the fractal grids and the streamwise upstream velocity U_∞, this Reynolds number value corresponds to a velocity of about 2.5 m/s in a wind tunnel at usual ambient conditions). The Reynolds number Re_M based on M_{eff} (and the same upstream velocity) is between 13 and 15 times larger than $Re_{t_{\min}} = 300$ depending on the grid, but the $t_r = 8.5$ fractal and the regular grids share the same value of Re_M. We have conducted a small study to investigate the influence of the Reynolds number in our flow configurations. We have run a DNS with a Reynolds number five time bigger (i.e. $Re_{t_{\min}} = 1{,}500$) than in the current work for the fractal grid with $t_r = 8.5$. We did not find any significant difference (less than 5%) on the quantities investigated in this paper in agreement with wind tunnel experiments (see Fig. 6 of [14]).

Inflow/outflow boundary conditions are used in the x-direction and periodic boundary conditions in the y direction for $-L_y/2$ and $L_y/2$ and in the z direction

$-L_z/2$ and $L_z/2$. The time step $\Delta t = 0.015 t_{\min}/U_\infty$ is low enough to have a CFL condition of about 0.75. It is important to stress that the three fractal grids differ only by their value of t_r, which given that they have same lengths L_j and same $t_{\min}$, determines all the differences. The streamwise position of the grid ($10t_{\min}$ from the inflow boundary of the computational domain) has been carefully chosen to avoid any spurious interactions between the modelling of the grid and the inflow boundary condition (see Fig. 4 for a schematic view of the flow configuration). The inflow profile is a uniform flow field U_∞ equal to 1 without any turbulence perturbations.

The number of mesh nodes is of crucial importance because all the scales need to be accurately represented. A preliminary study by [11] has shown that a discretisation of five mesh nodes across a distance $t_{\min}$ is enough to resolve the flow around the smallest bars of the fractal square grids at the Reynolds numbers considered here. This same study also established that the collection time needed in the simulations for well converged low order statistics is 750 $t_{\min}/U_\infty$. Statistics are obtained by exploiting the symmetries of the flow and by averaging over time at given spatial locations. This way, we obtain mean flow and turbulence profiles as functions of streamwise distance $x/t_{\min}$ and lateral coordinate $y/t_{\min}$.

3 Instantaneous flow visualisations

3D enstrophy visualisations of the turbulent flows generated by the regular grid and the three fractal square grids are shown in Figs. 5, 6, 7 and 8. In these figures we plot isosurfaces of the absolute value of the vorticity in blue and isosurfaces of the x-component of the vorticity in green. These isosurfaces are normalised in such a way that the decay of the turbulence is not visible on these plots. This decay is however

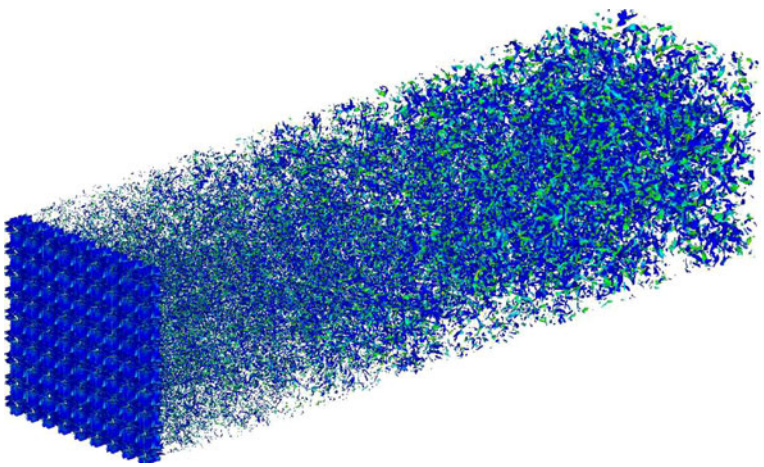

Fig. 5 Turbulent flow generated by the regular grid. Specifically, 3D isosurfaces of (in *blue*) the absolute value of the vorticity vector normalised by its maximum over the y-z plane at the x-position considered, and of (in *green*) the x-component of the vorticity normalised by its maximum over the y-z plane at the x-position considered. The value on both isosurfaces is 0.7

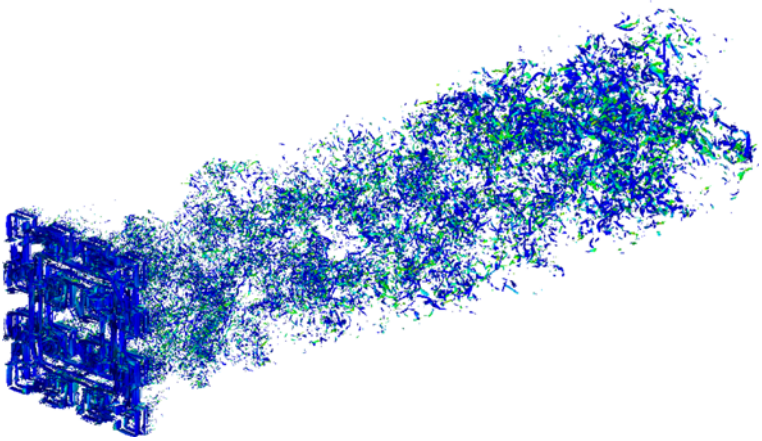

Fig. 6 Turbulent flow generated by the fractal square grid with $t_r = 5$. Same 3D plot as in Fig. 5

clearly visible in Fig. 9 where we plot the maximum of the enstrophy over every $(y - z)$ plane as a function of the streamwise coordinate x. Note that the turbulence-generating grid is placed at $x = 10t_{\min}$. It is clear from Fig. 9 that fractal grids generate higher vorticity values than the regular grid; compare in particular the curves for the regular grid and for the $t_r = 8.5$ grid as these two grids have the same blockage ratio.

The one obvious difference in these visualisations between the turbulent flow generated by the regular grid and the turbulent flows generated by the fractal square grids is that the latter are clearly more intermittent. The fact is also that these two different types of turbulent flows are generated in different ways. In the regular grid case, same-size wakes interact within a couple of mesh sizes from the grid and mix

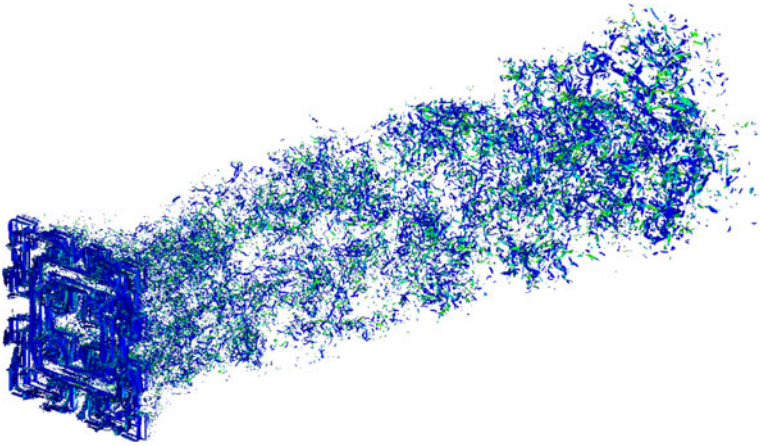

Fig. 7 Turbulent flow generated by the fractal square grid with $t_r = 6.5$. Same 3D plot as in Fig. 5

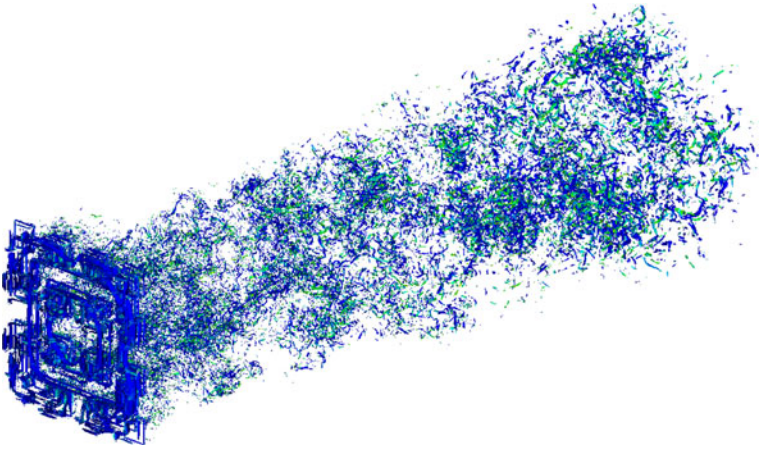

Fig. 8 Turbulent flow generated by the fractal square grid with $t_r = 8.5$. Same 3D plot as in Fig. 5

together in a uniform fashion close to the grid. In the fractal grid case, Laizet and Vassilicos [9] and Mazellier and Vassilicos [14] suggested that the smallest bars on the grid generate the smallest wakes which meet and mix together at the smallest distance from the grid, whereas larger bars generate larger wakes which meet and mix at a further distance from the grid, and that this process repeats itself from the smallest to the largest turbulent-generating scales on the grid in a way which causes the turbulence to progressively intensify over a protracted distance from the grid.

In the wind tunnel experiments [4, 14, 22] where fractal square grids with $N = 4$ iterations were used, this multiscale mode of turbulence generation causes the turbulence to progressively build up as it spatially homogenises at the same time. Turbulence profiles become homogeneous much further downstream than in the case of regular grids but turbulence intensities also amplify to much higher values

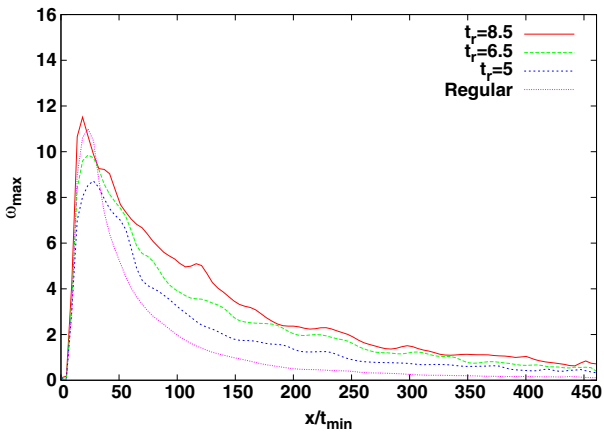

Fig. 9 Streamwise evolution of the maximum of the absolute value of the vorticity vector. The maximum is over the $y - z$ plane at a given x location

where the turbulence becomes homogeneous. It may be interesting to note that [23] suggest that fractal square grids can generate statistical homogeneous turbulence with different small-scale intermittency properties than homogeneous turbulence generated by regular grids.

We now provide some visual evidence for the multiscale wake interaction mechanism responsible for the turbulence generation by fractal square grids, and we then report on statistical homogeneity and isotropy and various turbulence profiles in Section 4.

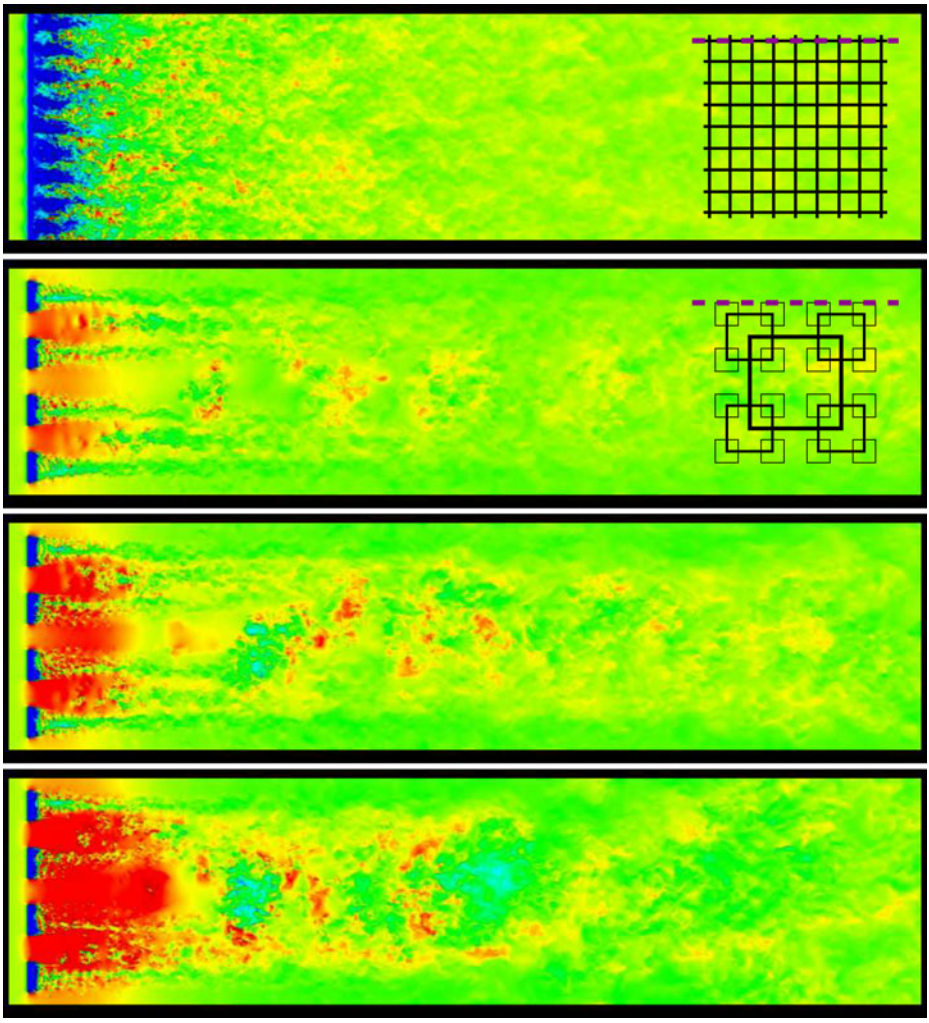

Fig. 10 Instantaneous streamwise velocity of the flow in the $(x - z)$ plane at $y/t_{\min} = 50.4$. The *blue regions* correspond to negative values for the streamwise velocity and the *red ones* to values above $1.5U_\infty$. From *top* to *bottom*: flow generated by the regular grid; $t_r = 5$ grid; $t_r = 6.5$ grid; and $t_r = 8.5$ grid

Figures 10, 11 and 12 illustrate our four turbulent flows by showing snapshots of instantaneous streamwise velocity fields at different y-z planes. These planes are indicated in the inserts inside these figures by red dotted lines against the grids. A very non-homogeneous turbulent field is obtained close to all grids, but in the case of the regular grid, the turbulence does homogenise relatively close to the grid. Instead, the turbulence remains non-homogeneous for a long distance downstream of the fractal grids. There is a clear presence of wakes of three different sizes in these figures, the smallest wakes being visible in Fig. 10, the intermediate size wakes being

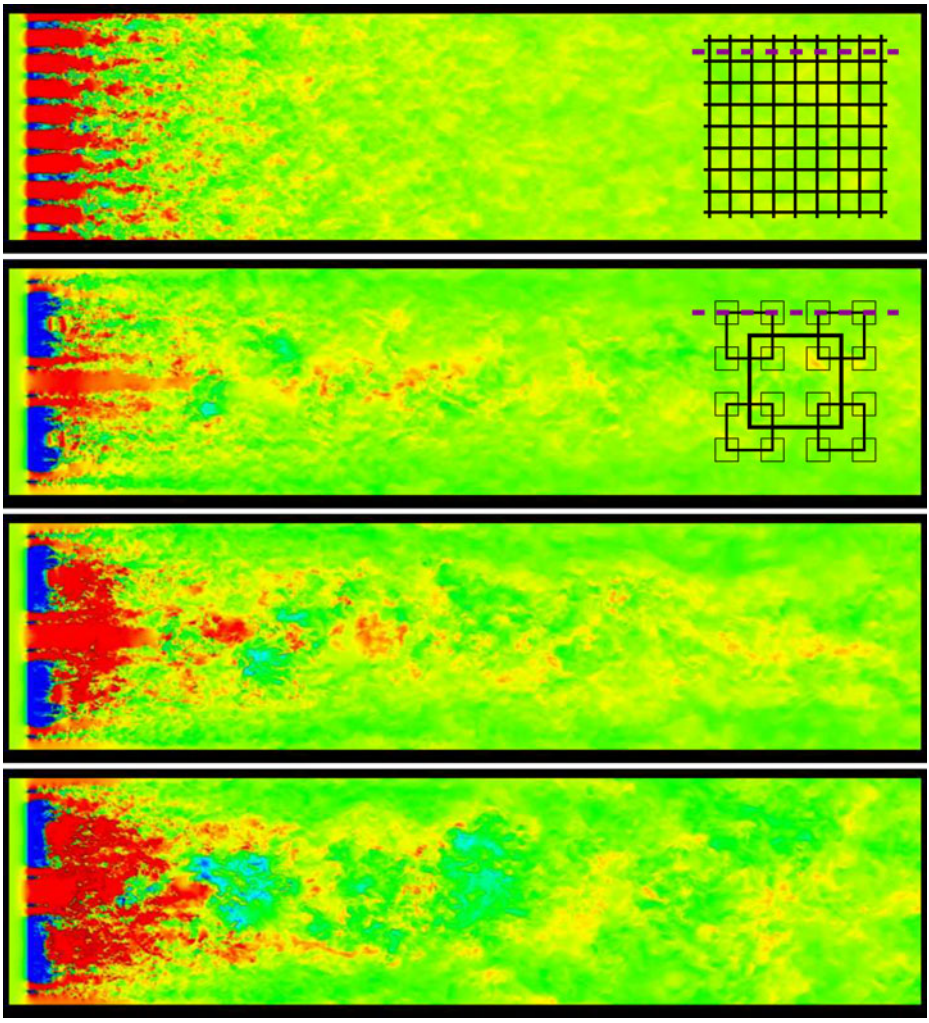

Fig. 11 Instantaneous streamwise velocity of the flow in the $(x - z)$ plane at $y/t_{\min} = 43.2$. The *blue regions* correspond to negative values for the streamwise velocity and the *red ones* to values above $1.5U_\infty$. From *top* to *bottom*: flow generated by the regular grid; $t_r = 5$ grid; $t_r = 6.5$ grid; and $t_r = 8.5$ grid

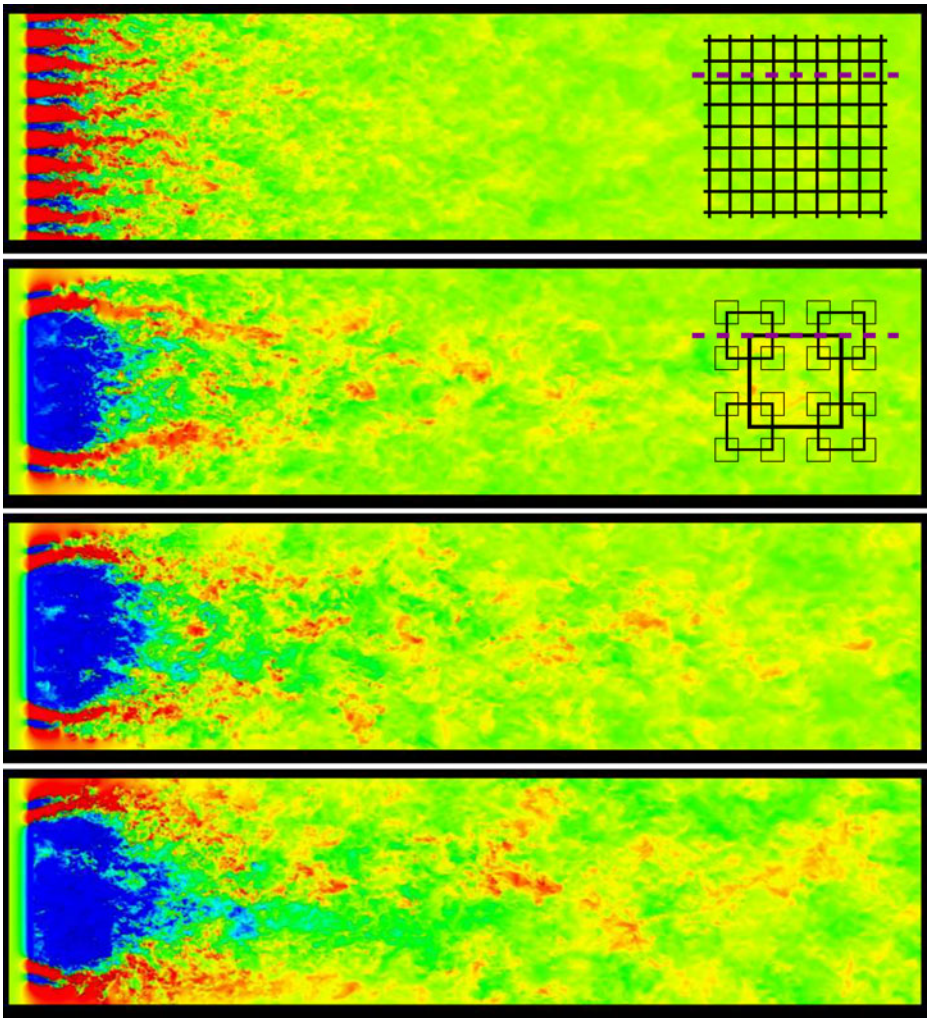

Fig. 12 Instantaneous streamwise velocity of the flow in the $(x - z)$ plane at $y/t_{\min} = 28.8$. The *blue regions* correspond to negative values for the streamwise velocity and the *red ones* to values above $1.5U_\infty$. From *top* to *bottom*: flow generated by the regular grid; $t_r = 5$ grid; $t_r = 6.5$ grid; and $t_r = 8.5$ grid

visible in Fig. 11 and the largest wakes being visible in Fig. 12. In Fig. 12, we observe a large recirculation area (in blue) in the wake of the biggest square of the fractal grids. However, as might have been expected, strong jet-like behaviours of various sizes are also present (in red). It is interesting to note that the smallest wakes on each side of the big one are oriented towards the lateral boundaries of the computational domain.

We also performed animations of the instantaneous enstrophy using 1,000 flow fields saved with a period of $0.3t_{\min}/U_\infty$ for a total duration of $300t_{\min}/U_\infty$. For the fractal square grids, the observation of the animations suggests that the streamwise

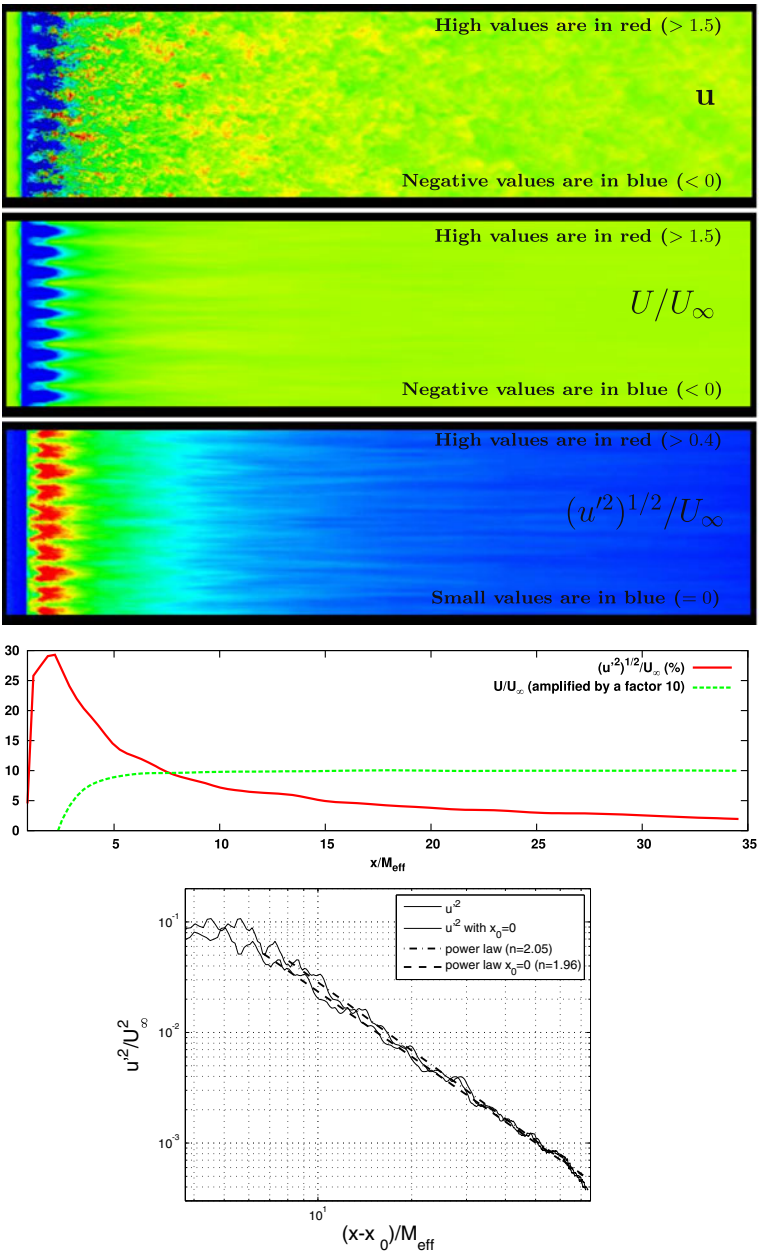

Fig. 13 From *top* to *bottom*: instantaneous streamwise velocity, its mean (U/U_∞) and turbulent ($(u'^2)^{1/2}/U_\infty$) components in the $x-y$ plane at $z=0$; streamwise evolution of U/U_∞ and $(u'^2)^{1/2}/U_\infty$ along the centreline ($z=y=0$); streamwise evolution of $(u'^2)/U_\infty^2$ along the centreline ($z=y=0$) using log-log coordinates. Two power-law fits are used, one where $x_0=0$ in $u'^2/U_\infty^2 \sim [(x-x_0)/M_{\text{eff}}]^{-n}$ and one which is a non-linear fit and which determines n and x_0 at the same time. Both give values of n very close to 2. Results obtained for the regular grid

locations where the different wakes interact are oscillating, following oscillations of the wakes themselves which are sometimes in and sometimes out of phase with each other.

4 Statistics

4.1 Mean flow and turbulence intensities

In Figs. 13, 14, 15 and 16, we plot the instantaneous streamwise velocity as well as its normalised mean (U/U_∞) and the normalised rms ($(u'^2)^{1/2}/U_\infty$) of the turbulent fluctuations obtained by averaging in time. As expected from previously reported wind tunnel measurements, the turbulent flow generated by a fractal grid is strongly

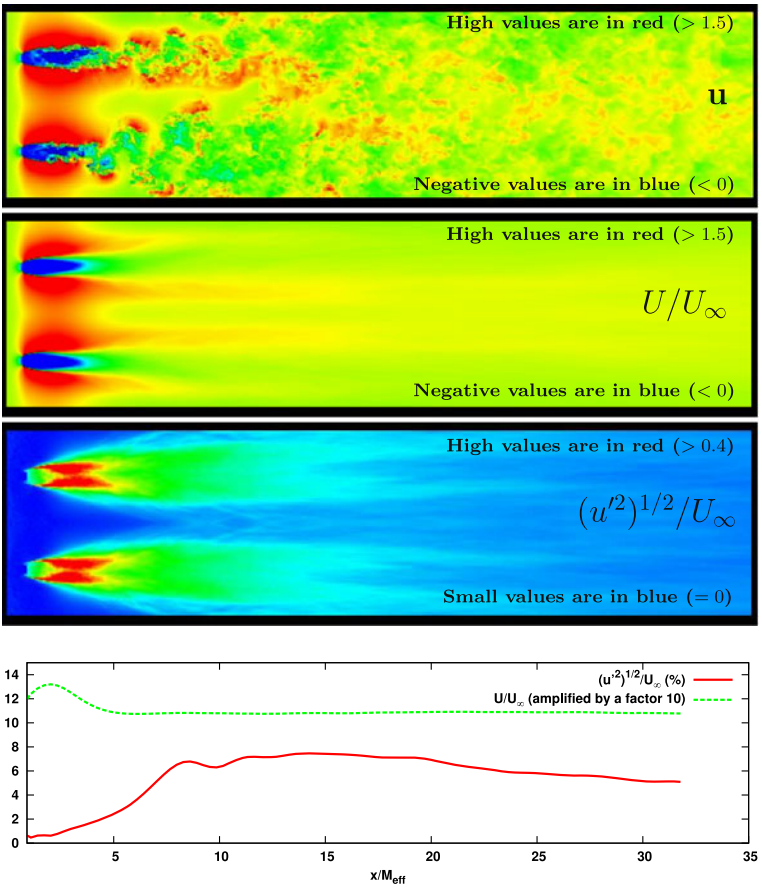

Fig. 14 From *top* to *bottom*: instantaneous streamwise velocity, its mean (U/U_∞) and turbulent ($(u'^2)^{1/2}/U_\infty$) components in the $x-y$ plane at $z=0$; streamwise evolution of U/U_∞ and $(u'^2)^{1/2}/U_\infty$ along the centreline ($z=y=0$). Results obtained for the $t_r=5$ grid

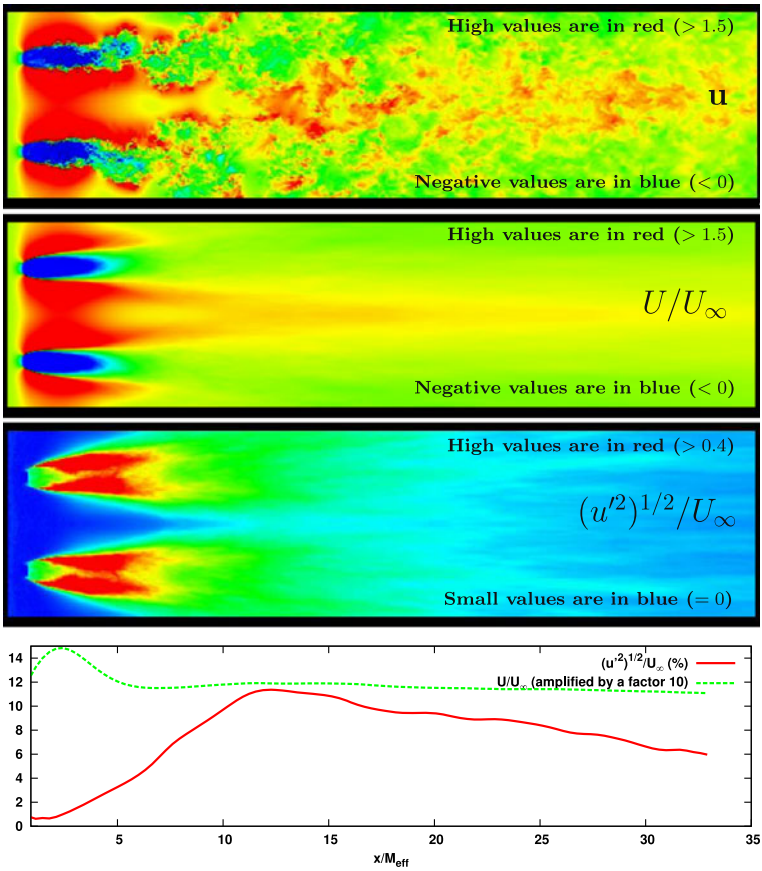

Fig. 15 From *top* to *bottom*: instantaneous streamwise velocity, its mean (U/U_∞) and turbulent ($(u'^2)^{1/2}/U_\infty$) components in the $x-y$ plane at $z=0$; streamwise evolution of U/U_∞ and $(u'^2)^{1/2}/U_\infty$ along the centreline ($z=y=0$). Results obtained for the $t_r=6.5$ grid

influenced by the aspect ratio t_r of the grid. For the mean component of the streamwise velocity, the main feature is that the red regions, corresponding to values above $1.5U_\infty$ are more extended when t_r, and therefore σ, is increased, especially near the centreline of the grid. The increasing jet-like area contributes to an increase of the values of the corresponding turbulent component in the domain of our simulations. Indeed, for the $t_r=8.5$ grid, the area in green is much bigger than for the $t_r=5$ grid. It should be noticed as well that the recirculation areas in blue in the mean flow plots seem to be increasingly orientated towards the lateral boundary limits of the computational domain for increasing t_r, which is consistent with the increasingly high-speed character of the flow near the centreline of the grid. Furthermore, it seems that the flow is less homogeneous far downstream from the grid when t_r, and therefore σ in this context, are increased. In contrast, Hurst and Vassilicos [4] found that the turbulence actually becomes more homogeneous far downstream when t_r is increased whilst keeping σ constant.

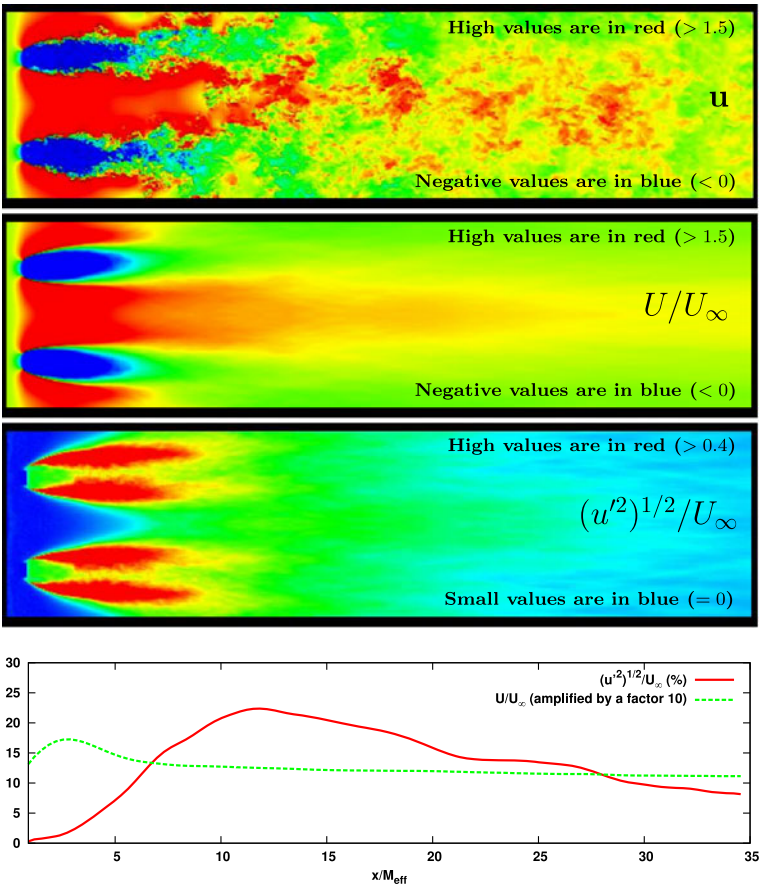

Fig. 16 From *top* to *bottom*: instantaneous streamwise velocity, its mean (U/U_∞) and turbulent ($(u'^2)^{1/2}/U_\infty$) components in the $x-y$ plane at $z=0$; streamwise evolution of U/U_∞ and $(u'^2)^{1/2}/U_\infty$ along the centreline ($z=y=0$). Results obtained for the $t_r=8.5$ grid

In the regular grid case, the centreline $y=z=0$ cuts through the crossing of two bars on the grid. As a result, close to the grid along this line, U/U_∞ is found to have a wake-like behaviour with a small recirculation bubble where U/U_∞ takes negative values up to $x/t_{\min}\approx 25$ (which corresponds to $x/M_{\text{eff}}\approx 2$, see fourth plot from top in Fig. 13). The centreline $y=z=0$ does not cross a bar in the case of our three fractal square grids, so U/U_∞ is found to have a jet-like behaviour with a peak around $x/t_{\min}\approx 20$ followed by a smooth decay toward a value which remains larger than 1 and tends towards 1.2 within our computational domain after $x\approx 200t_{\min}$, see Figs. 14–16. In these figures one can also clearly see the influence of the aspect ratio t_r, or equivalently of the blockage ratio σ: the maximum value for U/U_∞ is about 1.3 for the $t_r=5$ grid and about 1.75 for the $t_r=8.5$ grid.

In fact, both wake-like and jet-like behaviours can be observed at different lateral locations in the lee of the three fractal grids, as evidenced by Figs. 10, 11 and 12.

We find recirculation bubble-type x-dependencies of U/U_∞ along lines orthogonal to the $y-z$ plane but crossing a bar on the fractal grid (not plotted here). Along such lines, U/U_∞ peaks at values above 1 after these recirculation bubbles and subsequently decays towards values which remain below 1 with increasing x. These observations suggest that the mean flow is not homogeneous downstream of the fractal grids for the extent of our computational domain which is not longer than about $35M_{\mathrm{eff}}$ (the wind tunnel experiments of [4] detected homogeneity at much further distances downstream for the fractal square grids they used). Of course, we checked that $\frac{1}{L_y L_z}\int_{-L_y/2}^{L_y/2}\int_{-L_z/2}^{L_z/2} u dy dz = U_\infty$ by integrating over many $y-z$ planes normal to the streamwise direction.

The presence of longitudinal gradients of U causes turbulence production, and indeed, as seen in the bottom plots of Figs. 13–16, the fractal grids generate much higher intensities than the regular grid, except very close to the grid where the regular grid generates the highest intensities. As expected, the turbulence intensity increases with increasing σ, i.e. with increasing t_r in the case of the present fractal grids. Perhaps more interesting may be the observation that the turbulence intensity peaks at a large number of mesh sizes away from the fractal grids in qualitative agreement with the wind tunnel experiments of [4] (see Fig. 35a of their paper), even though low-blockage fractal square grids with $N = 4$ iterations were actually used in these experiments.

Another interesting observation which we report at the bottom of Fig. 13 is that $\frac{u'^2}{U_{\infty^2}} \approx \left(\frac{x-x_0}{M_{\mathrm{eff}}}\right)^{-2}$ seems to be a good fit of the turbulence decay far enough downstream of the regular grid used in our simulation. It is well known that $\frac{u'^2}{U_{\infty^2}} \approx \left(\frac{x-x_0}{M_{\mathrm{eff}}}\right)^{-2.5}$ in the final period of decay when the Reynolds number (based on the Taylor microscale) has decayed to such a small value that the non-linearity in the Navier-Stokes equations is negligible [1]. At high Reynolds numbers, $\frac{u'^2}{U_{\infty^2}} \approx \left(\frac{x-x_0}{M_{\mathrm{eff}}}\right)^{-n}$ with an exponent n which is smaller or equal to 10/7 or about 1.5 in practice [16]. The Reynolds number for the regular grid in the present simulation is low, too low for such values of n, but not low enough for $n = 2.5$ as in the final period of decay.

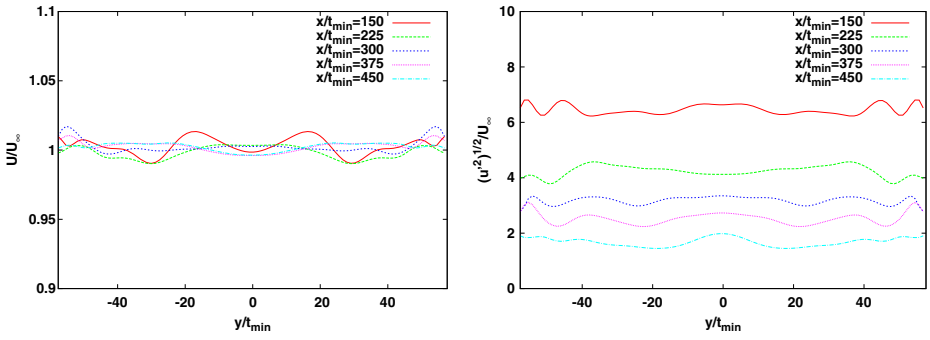

Fig. 17 Lateral evolution of U/U_∞ (*left*) and $(u'^2)^{1/2}/U_\infty$ (*right*) for the regular grid at five different streamwise locations where $z = 0$

In the regular grid case mean streamwise velocity and turbulence intensity profiles along y become approximately homogeneous as one moves downstream and x exceeds values about $20M_{\text{eff}}$ or so, i.e. above about $300t_{\min}$ (see Fig. 17). However, the mean flow profiles are quite different in the lee of our three fractal square grids. Figures 18, 19 and 20 show the streamwise evolutions of three mean velocity profiles and three turbulence intensity profiles downstream of the fractal grids. It is clear that the mean flow is not homogeneous for the entire downstream extent of our simulations. It is also interesting to note that the lateral mean velocities V and W are significantly non-zero and that their signs imply the existence of mean flow away from the centreline along the $y = 0$ and $z = 0$ axes (by symmetry, $V < 0$ is

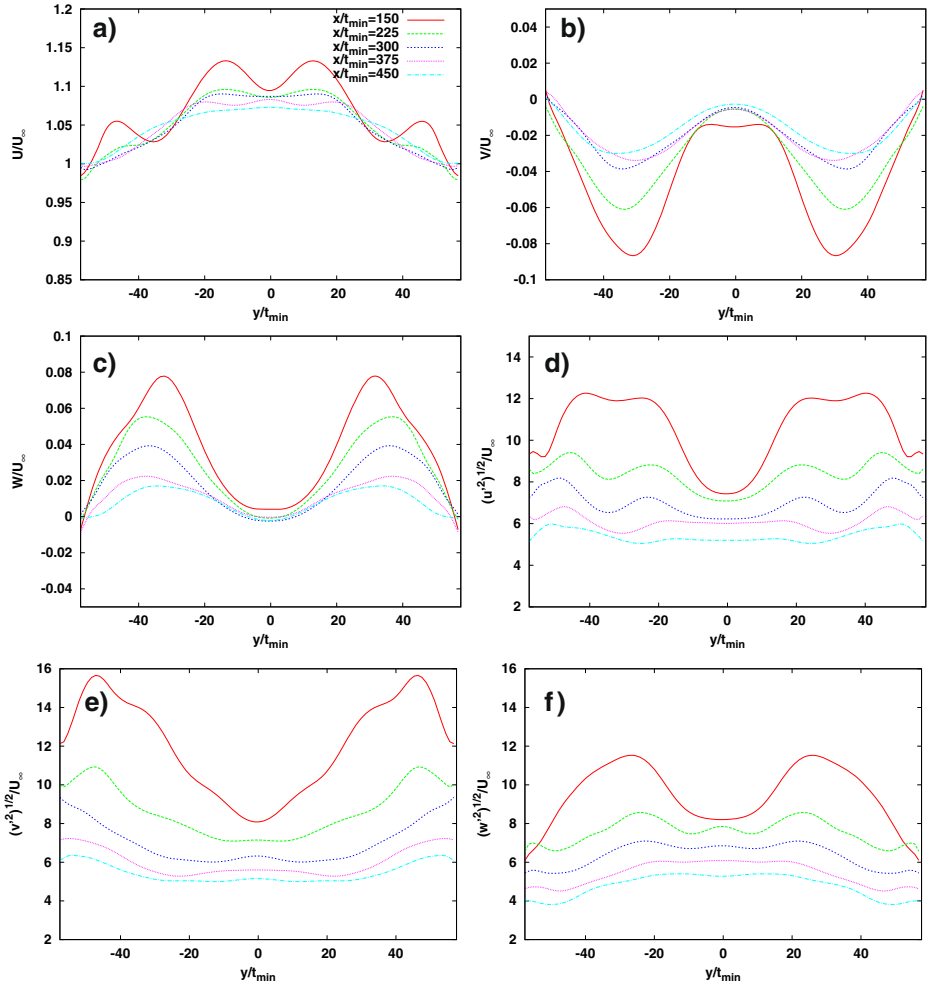

Fig. 18 Lateral evolution of: **a** U/U_∞, **b** V/U_∞, **c** W/U_∞, **d** $(u'^2)^{1/2}/U_\infty$, **e** $(v'^2)^{1/2}/U_\infty$, **f** $(w'^2)^{1/2}/U_\infty$, for the $t_r = 5$ grid at five different streamwise locations where $z = 0$

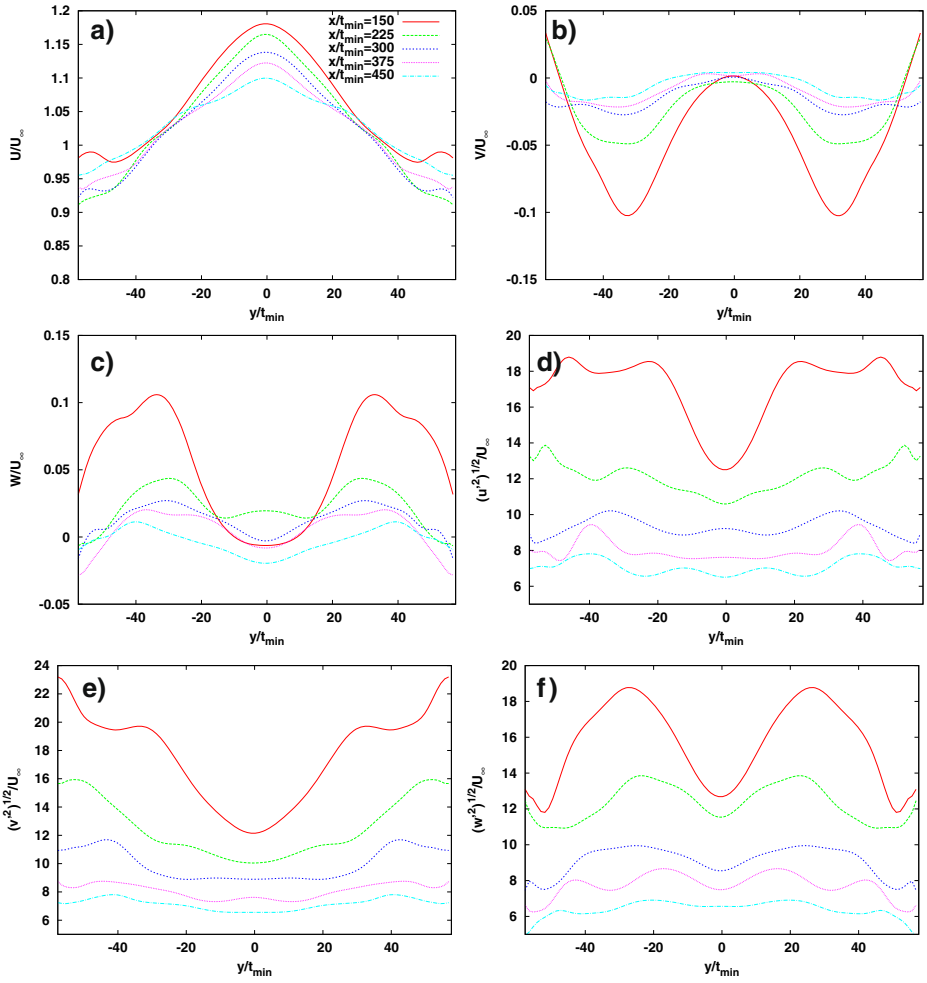

Fig. 19 Lateral evolution of: **a** U/U_∞, **b** V/U_∞, **c** W/U_∞, **d** $(u'^2)^{1/2}/U_\infty$, **e** $(v'^2)^{1/2}/U_\infty$, **f** $(w'^2)^{1/2}/U_\infty$, for the $t_r = 6.5$ grid at five different streamwise locations where $z = 0$

equivalent to $W > 0$). In agreement with mass conservation, we have checked that there is mean flow towards the centreline along the $y = z$ and $y = -z$ intermediate lines.

The turbulence intensities, whilst also inhomogeneous for much of the way downstream, may seem to approximately homogenise towards the end of the simulation domain. However, Fig. 21 shows clearly that the Reynolds stresses remain highly inhomogeneous all the way. In Fig. 22 we also plot isotropy indicators u'/v', u'/w' and v'/w' of the large-scale turbulent fluctuations as they evolve downstream along the centreline. These indicators lie approximately between 0.8 and 1.2. Note that our values of u'/v' agree with the experimental results of [4] who also found that, on the centreline, u'/v' is always above 1 with values between 1.2 and 1.3 for all the fractal

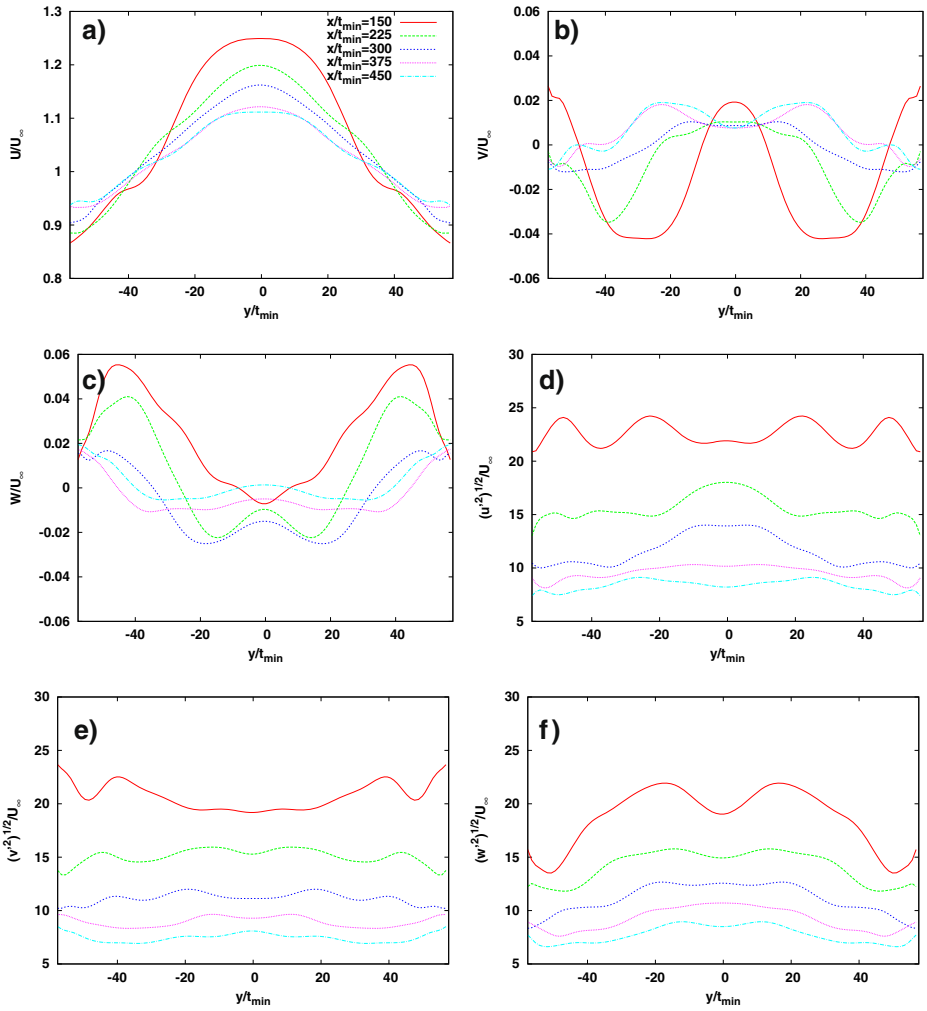

Fig. 20 Lateral evolution of: **a** U/U_∞, **b** V/U_∞, **c** W/U_∞, **d** $(u'^2)^{1/2}/U_\infty$, **e** $(v'^2)^{1/2}/U_\infty$, **f** $(w'^2)^{1/2}/U_\infty$, for the $t_r = 8.5$ grid at five different streamwise locations where $z = 0$

square grids they studied. Note also that the constant evolution of v'/w' along the centreline with a value very close to 1 reflects the symmetry of the flow.

A more complete picture can be obtained by plotting the three mean velocities and a turbulence intensity on $(y - z)$ planes placed at different streamwise distances x, see Fig. 23 for the regular grid and Figs. 24, 25 and 26 which correspond to the three fractal grids. The red regions correspond to large positive values and the blue regions indicate negative values in the mean flow plots but zero values in the turbulence intensity plots. The fractal grids have very distinct geometrical imprints on the mean flow properties. So does the regular grid, but it loses its imprint quite early on, i.e. a very dim imprint is left by $x = 100t_{\min}$, whereas the imprints of

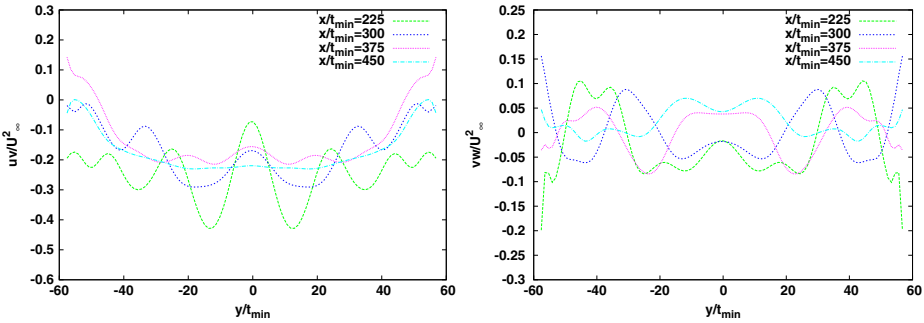

Fig. 21 Lateral evolution of $< u'v' > /U_\infty^2$ (*left*) and $< v'w' > /U_\infty^2$ (*right*), for the $t_r = 8.5$ grid at five different streamwise locations where $z = 0$

the fractal grids are still visible and intense till $x = 100t_{\min}$ and beyond. Figure 27 shows the evolution of this geometrical imprint on the streamwise mean flow and turbulence intensity beyond $x = 100t_{\min}$ for the case of the $t_r = 8.5$ fractal square grid. Even though the red to blue regions correspond to a smaller range of values by comparison to the previous four figures, a clear geometrical imprint survives till

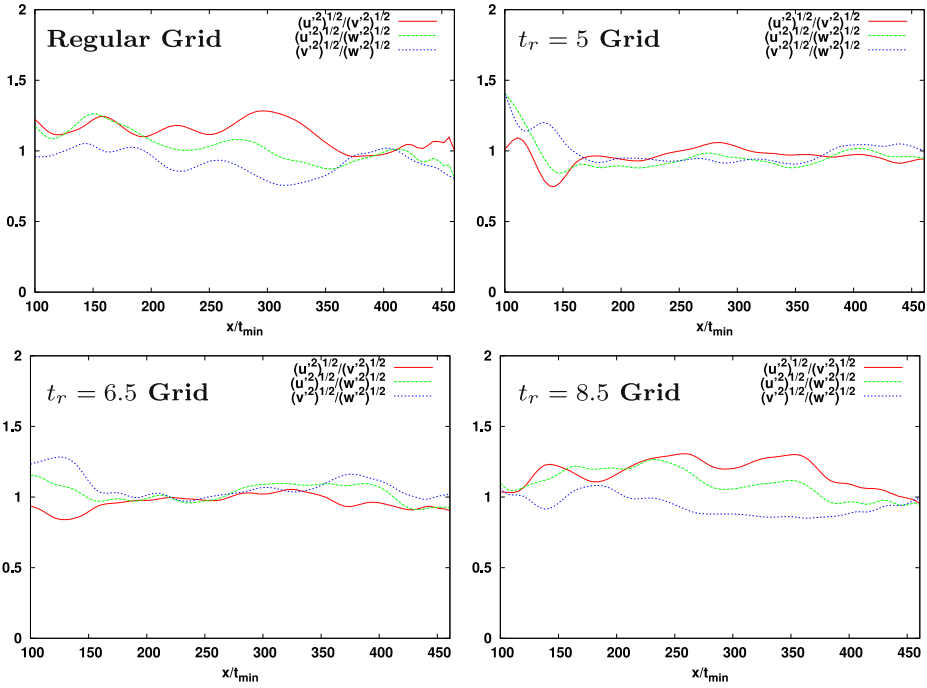

Fig. 22 Streamwise evolution of the large-scale isotropy indicators u'/v', u'/w' and v'/w' for the four simulations

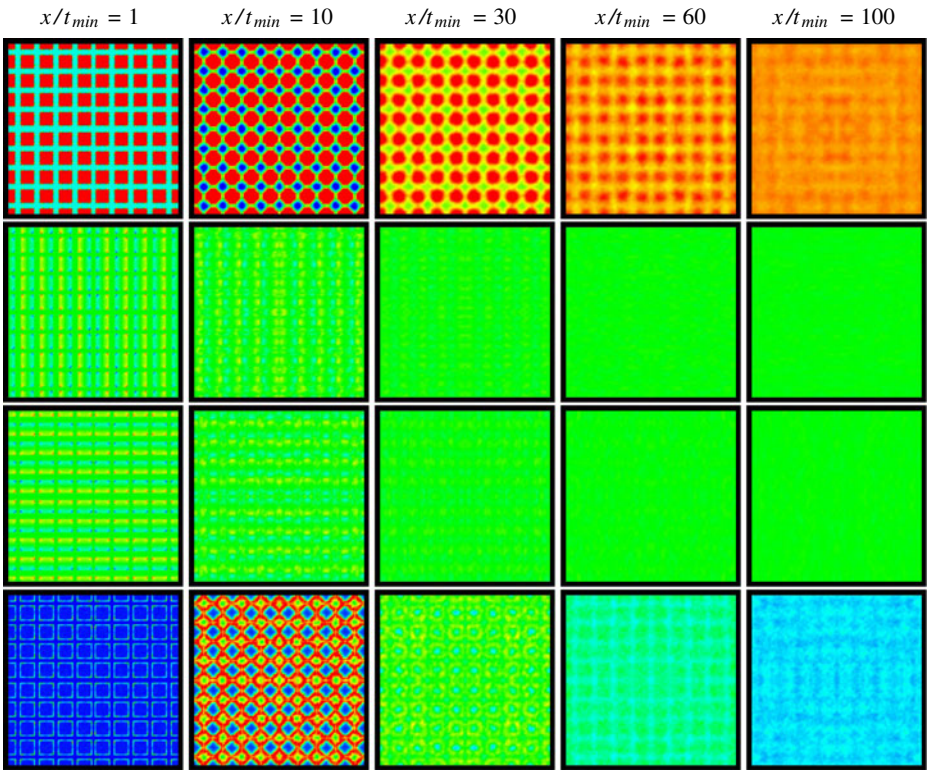

Fig. 23 From *top* to *bottom*: Streamwise evolution of U/U_∞ (−0.5 in *blue*, 1.25 in *red*), V/U_∞ (−0.5 in *blue*, 0.5 in *red*), W/U_∞ (−0.5 in *blue*, 0.5 in red) and $(u'^2)^{1/2}/U_\infty$ (0 in *blue*, 0.5 in *red*) for the regular grid

the end of our simulation domain. Note that the turbulence intensity decays quite fast and therefore the red colour corresponds to diminishing values for increasing downstream positions.

The observation of such persistent geometrical imprints in the mean flow properties has quite an interesting consequence. The equation for the turbulent fluctuating velocity field $\mathbf{u}'$ is

$$\frac{\partial}{\partial t}\mathbf{u}' + \mathbf{u}' \cdot \nabla \mathbf{u}' = -\frac{1}{\rho}\nabla p' + \nu \nabla^2 \mathbf{u}' + \frac{1}{\rho}\mathbf{f} \tag{1}$$

where $\mathbf{f}$ acts, effectively, as a body forcing determined by mean turbulent flow profile statistics as follows

$$\frac{1}{\rho}\mathbf{f} = \frac{\partial}{\partial x_j} < u_j' \mathbf{u}' > -\mathbf{U} \cdot \nabla \mathbf{u}' - \mathbf{u}' \cdot \nabla \mathbf{U} \tag{2}$$

Similarly to the Coriolis force, $\mathbf{f}$ depends on $\mathbf{u}'$, but unlike the Coriolis force, $\mathbf{f}$ can actually do work on the turbulent fluctuating velocity $\mathbf{u}'$. As this body force $\mathbf{f}$ is determined, in part, by the one-point mean flow and Reynolds stress profiles of the

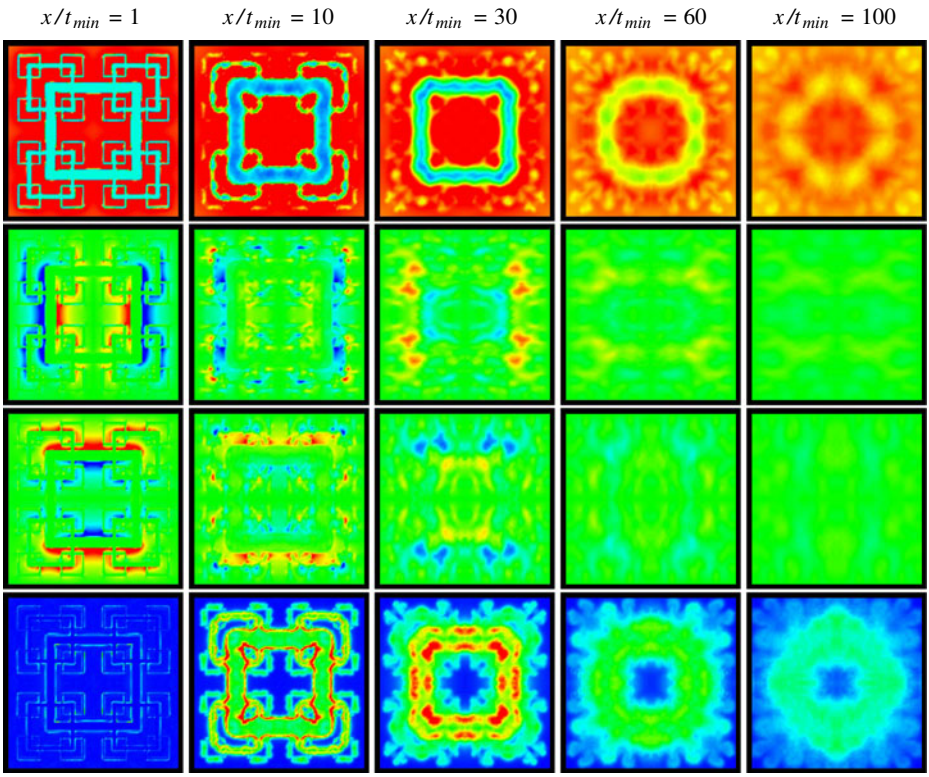

Fig. 24 From *top* to *bottom*: Streamwise evolution of U/U_∞ (-0.5 in *blue*, 1.25 in *red*), V/U_∞ (-0.5 in *blue*, 0.5 in *red*), W/U_∞ (-0.5 in *blue*, 0.5 in *red*) and $(u'^2)^{1/2}/U_\infty$ (0 in *blue*, 0.5 in *red*) for the $t_r = 5$ grid

turbulence, and as these profiles bare a clear persistent imprint of the multiscale geometry of the fractal grid which generates the turbulence, it may seem reasonable to expect that the multiscale grid geometry could have a persistent effect on the two-point statistics and interscale energy transfers of the turbulent fluctuating velocity field. Mazzi and Vassilicos [15] showed how a persistent multiscale body forcing can deeply alter the two-point and interscale transfer structures of the turbulence, but in the idealised context of a periodic DNS of stationary, homogeneous and isotropic turbulence. However, the length-scales operated by the forcing and the length-scales of the turbulence overlap in their DNS. There may be some such overlap in some fractal/multiscale-generated turbulence which may persist far downstream, in which case one might expect quite unusual interscale turbulence dynamics, including the possibility of effectively negative eddy viscosities as pointed out by [13].

There is also the possibility that some aspects of the unusual interscale dynamics generated by the multiscale body forcing **f** on the turbulent fluctuations persist further downstream than the body forcing itself. Such an effect could help explain the unique turbulence decay properties observed by [4, 22] and [14] in the decay region very far downstream. This is the region where the turbulence has become

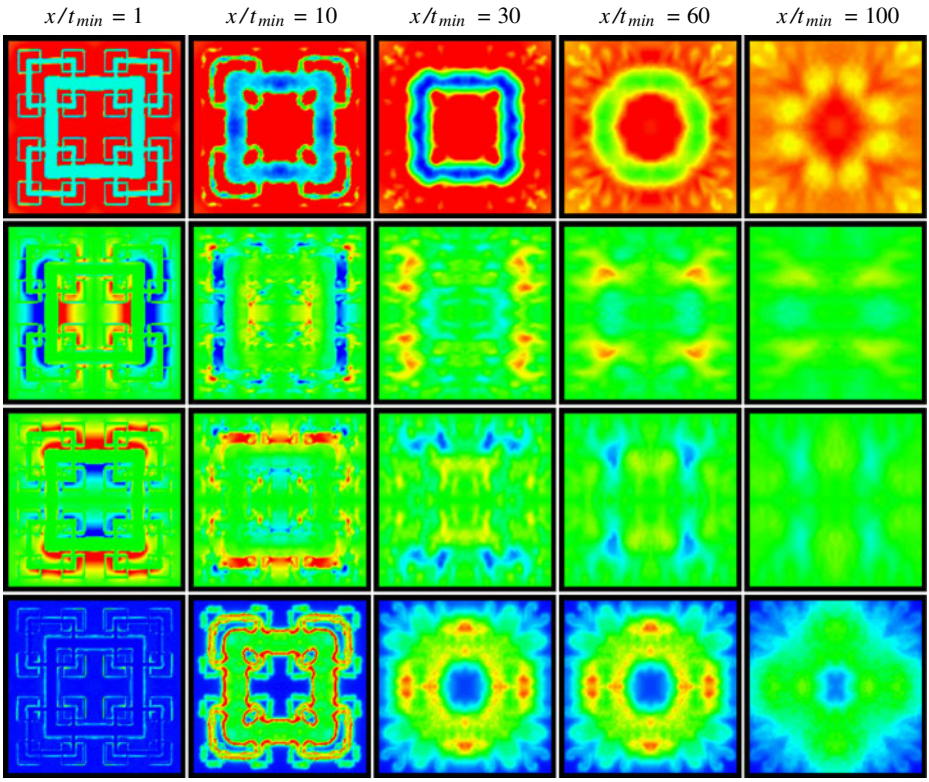

Fig. 25 From *top* to *bottom*: Streamwise evolution of U/U_∞ (-0.5 in *blue*, 1.25 in *red*), V/U_∞ (-0.5 in *blue*, 0.5 in *red*), W/U_∞ (-0.5 in *blue*, 0.5 in *red*) and $(u'^2)^{1/2}/U_\infty$ (0 in *blue*, 0.5 in *red*) for the $t_r = 6.5$ grid

homogeneous and the turbulence fluctuations decay freely. The results of the wind tunnel experiments of these authors indicate that homogeneity is reached beyond $x = 800t_{\min}$ with fractal square grids which, however, have $N = 4$, not $N = 3$, fractal iterations.

In summary, our results open up possibilities for generating and investigating such interscale dynamics but we must leave them for future study. In the next subsection we investigate the nature of the turbulence intensity peak.

4.2 Turbulence intensity peak

Perhaps the most salient property of the turbulence generated by fractal square grids is the protracted production region immediately after the grid where the turbulence continuously intensifies reaching a turbulence intensity peak at a far point beyond which the turbulence decays. This has been observed in wind tunnel experiments [4, 14] for low blockage fractal square grids and along various straight lines in the streamwise direction.

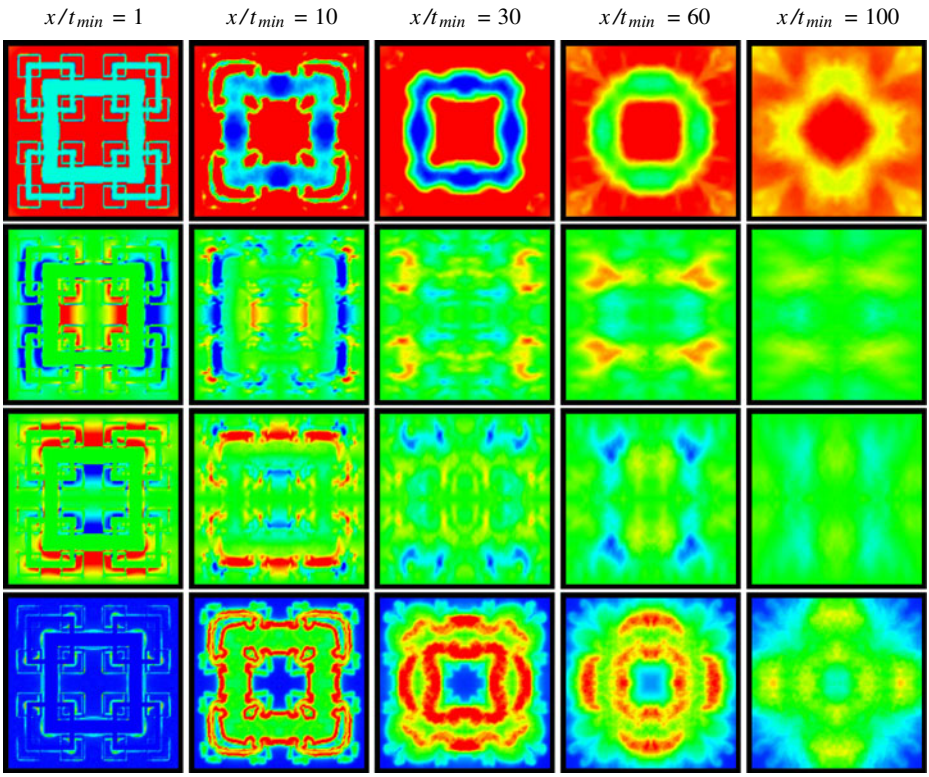

Fig. 26 From *top* to *bottom*: Streamwise evolution of U/U_∞ (-0.5 in *blue*, 1.25 in *red*), V/U_∞ (-0.5 in *blue*, 0.5 in *red*), W/U_∞ (-0.5 in *blue*, 0.5 in *red*) and $(u'^2)^{1/2}/U_\infty$ (0 in *blue*, 0.5 in *red*) for the $t_r = 8.5$ grid

In particular, it was shown by these wind tunnel experiments that the furthest peak point is the one on the centreline. As explained in [14], the furthermost interaction between wakes will be that of the wakes generated by the largest bars placed furthermost on the fractal grid, as shown in Fig. 28. Previous DNS of turbulent flows generated by fractal square grids have also demonstrated this mechanism but not on the centreline and for low blockage grids [7, 9]. Here we clearly confirm the streamwise production of turbulence for low to moderate blockage fractal square grids and on the centreline, which is important as it means that our DNS reaches into some of the region beyond the peak where the turbulence decays along all streamwise lines. One can see in Fig. 29 how, for all three of our fractal square grids, u'/U_∞ builds up along the centreline ($y/t_{tmin} = z/t_{\min} = 0$) until it reaches a point x_{peak} where it peaks and then eventually decays beyond that point. One can also see in Fig. 30 how u'/U_∞ peaks at different streamwise locations along streamwise lines crossing the grid at different lateral locations. There are clear wake-like behaviours where this location is on a blocking bar and more jet-like behaviours where this location is on an empty region of the grid. It is also clear from this picture that the furthest peak point is the one on the centreline.

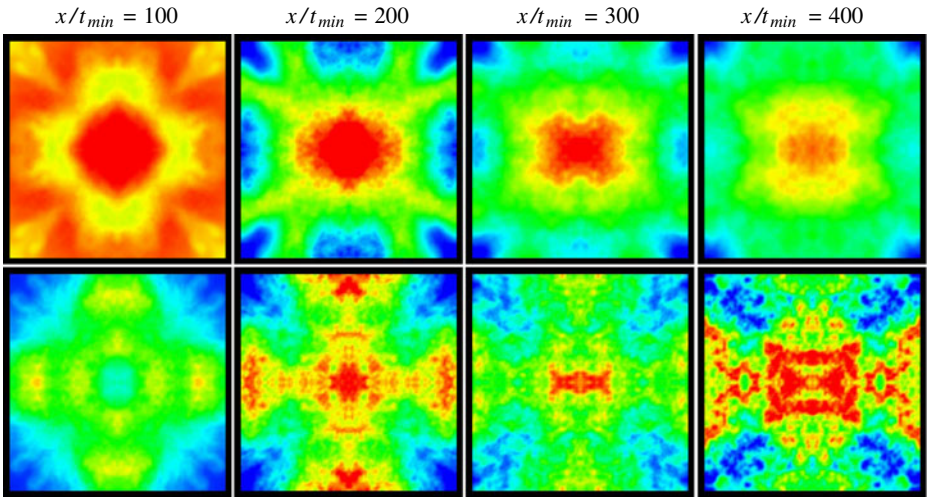

Fig. 27 From *top* to *bottom*: Streamwise evolution of U/U_∞ (0.85 in *blue*, 1.15 in *red*) and $(u'^2)^{1/2}/U_\infty$ (0.06 in *blue*, and from *left to right* 0.4, 0.2, 0.15, 0.1 in *red*), for the $t_r = 8.5$ grid in the far downstream region from the grid

It may be interesting to constrast the streamwise turbulence intensity behaviours in the lee of our fractal grids with our regular grid where the behaviour is almost the same everywhere (with expected differences very near the grid depending on whether the location probed is behind or between bars) and displays a marked decay beyond about $x \approx 10t_{\min}$. At the end of the computational domain, the regular grid returns $(u'^2)^{1/2}/U_\infty \approx 2.5\%$ whereas we have much larger turbulence intensities from the fractal square grids even when their blockage ratio is smaller.

The wind tunnel experiments [4, 14] showed that x_{peak} differs for different fractal grids and [14] proposed the formula

$$x_{\text{peak}} \approx 0.45 \frac{L_0^2}{t_0} \tag{3}$$

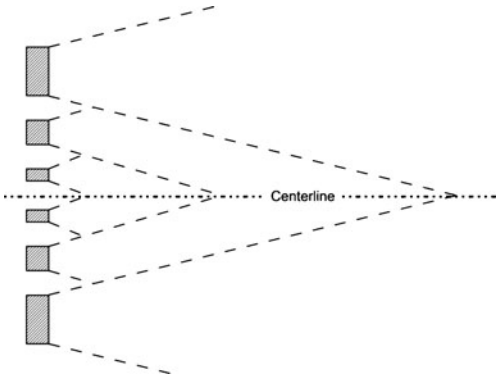

Fig. 28 Schematic explanation of wake interactions resulting from the fractal grids bars (from [14])

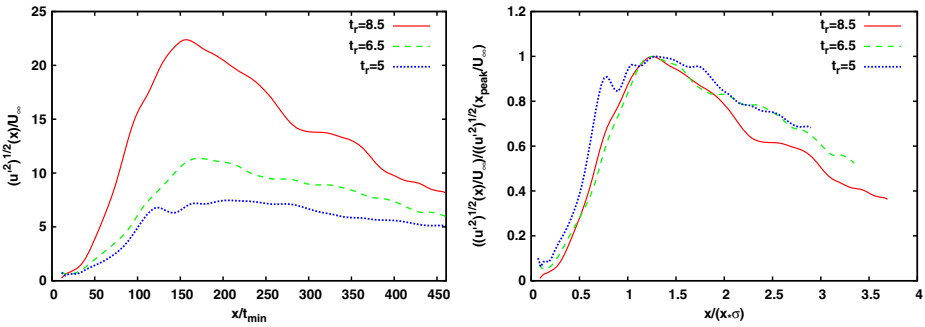

Fig. 29 Streamwise evolution of $(u'^2)^{1/2}/U_\infty$ on the centreline of the three fractal grids

for the furthest x_{peak}, i.e. along the centreline. This is an important formula as it shows how a salient bespoke feature of such turbulent flows can be manipulated and designed at will. However, it was obtained for low blockage fractal square grids ($\sigma = 25\%$) with $N = 4$ fractal iterations whereas our present grids have only $N = 3$ fractal

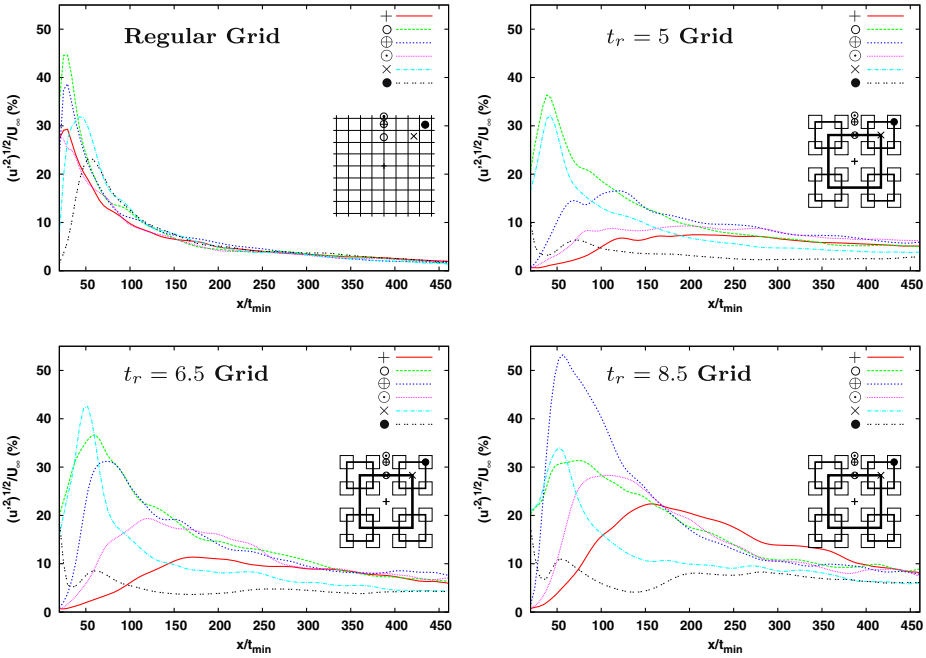

Fig. 30 Streamwise evolution of $(u'^2)^{1/2}/U_\infty$ at different lateral locations for the four simulations: $+$ corresponds to $y/t_{\min} = 0$, $z/t_{\min} = 0$, $\times$ to $y/t_{\min} = 28.8$, $z/t_{\min} = 28.8$, $\bullet$ to $y/t_{\min} = 43.2$, $z/t_{\min} = 43.2$, $\otimes$ to $y/t_{\min} = 0$, $z/t_{\min} = 28.8$, $\oplus$ to $y/t_{\min} = 0$, $z/t_{\min} = 43.2$ and $\odot$ to $y/t_{\min} = 0$, $z/t_{\min} = 50.4$

iterations and blockage ratios which vary from $\sigma = 23$–32%. It is therefore important to note that our simulations confirm the wind tunnel experiments concerning the existence of x_{peak} even if the number of fractal iterations is smaller than in the experiments and even if the values of σ differ. However, the formula for x_{peak} proposed by [14] does not fit our results.

As explained and visually confirmed in the previous section, the turbulence generated downstream of the fractal grids results from the interactions between the wakes of the different-size bars. Because these bars have different sizes and are placed at different distances from each other in accordance with their sizes, their wakes interact at different distances from the grid. The furthest such distance is for the largest bars and their wake size is proportional to $\sqrt{t_0 x}$ at a distance x from the grid [24]. However, the proportionality coefficient will be greater if the turbulence surrounding the wake is more intense as one might expect if a wider range of bar thicknesses, including larger ones, is present on the grid. In that case, this proportionality coefficient will be smaller for $N = 3$ than for $N = 4$ thus giving the first cause for a deviation from $x_{\text{peak}} \approx 0.45 \frac{L_0^2}{t_0}$. This deviation should be towards a coefficient larger than 0.45 in the proportionality between x_{peak} and $\frac{L_0^2}{t_0}$ because the wakes should be less wide (i.e. smaller size at a given x) for $N = 3$ and therefore meet further downstream than for $N = 4$ (see argumentation surrounding the wake interaction length-scale in [14]).

However, there is also a second cause for deviation, and this is the difference in blockage ratio. One might expect an increased blockage ratio to increase and accelerate the streamwise mean flow through the reduced large opening at the centre of the fractal grid and thereby also accelerate the lateral mean flow towards the centreline by incompressibility. This acceleration of the streamwise mean flow is followed by a deceleration a little further downstream (see Figs. 13–16) where one could expect the mean lateral flow to reverse away from the centreline and thereby deflect the wakes of the largest bars away from the centre. This is confirmed in Fig. 31 where we plot selected mean streamlines for each grid. As the blockage ratio is increased, the recirculation regions behind the largest bars on the fractal square grids increase in size and the mean streamlines upstream of them deviate towards the lateral boundaries of the computational domain. This deviation adds to the tendency for the wakes from the largest bars to meet further downstream with increasing σ, and must therefore significantly contribute to the increase of the coefficient of proportionality between x_{peak} and $\frac{L_0^2}{t_0}$. Hence, we expect the position x_{peak} on the centreline to be given by

$$x_{\text{peak}} = C(N, \sigma) x_\star = C(N, \sigma) \frac{L_0^2}{t_0} \tag{4}$$

where the dimensionless coefficient $C(N, \sigma)$ is an increasing function of σ (because of the above second cause for deviation) and, under the right conditions regarding the distribution of length-scales on the fractal grid, a decreasing function of N (because of the above first cause for deviation). In Fig. 29 (right), we plot $(u'^2)^{1/2}/U_\infty$ normalised by its value at x_{peak} as a function of $x/(x_\star \sigma)$. For our limited range of only three fractal square grids, and the very limited resulting range of σ, $C(3, \sigma) \approx \frac{5}{4}\sigma$ seems to give an ad hoc fit of the data. However, there is no strong reason to expect that $C(N, \sigma)$ should be proportional to σ.

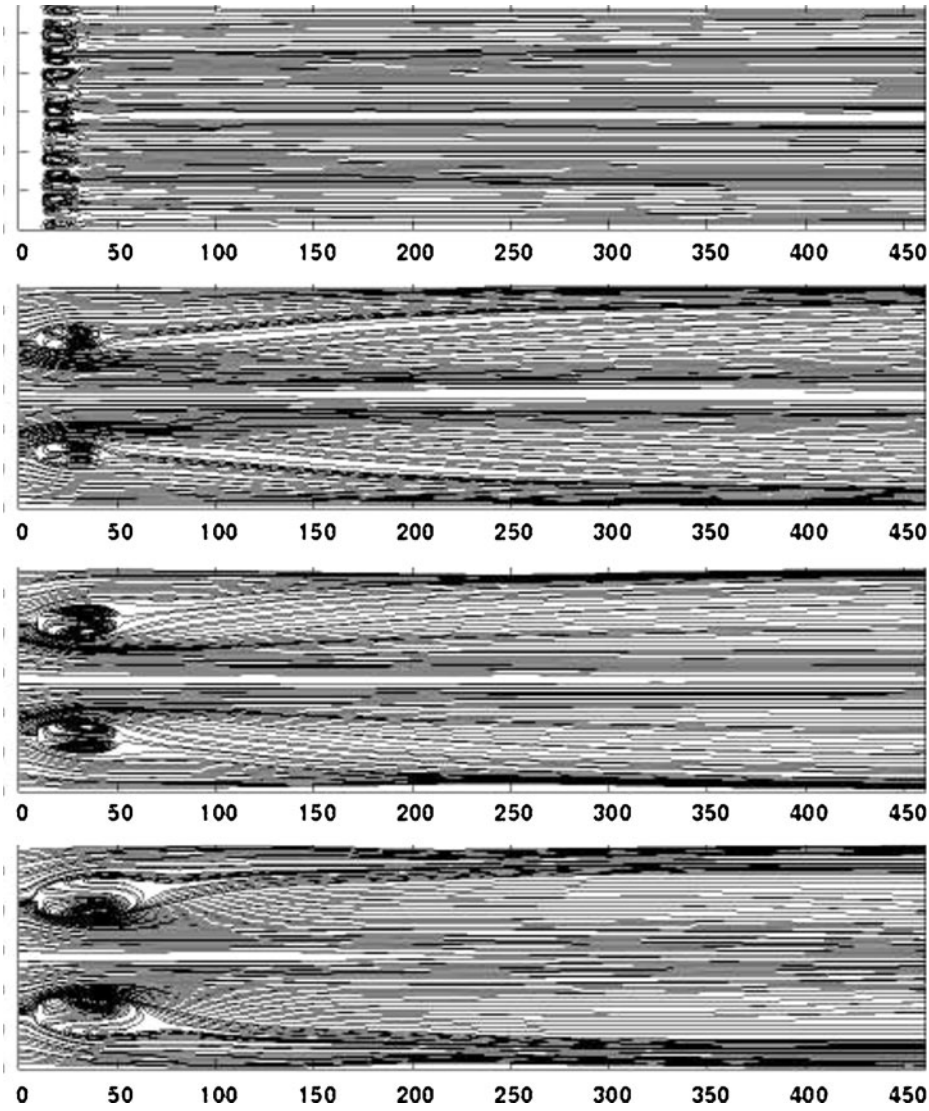

Fig. 31 Mean velocity streamlines for each simulation in the $(x - y)$ plane for $z = 0$. From *top to bottom*: regular grid, $t_r = 5$ grid, $t_r = 6.5$ grid and $t_r = 8.5$ grid

It must be noted that, unlike the wind tunnel experiments of [4, 14] where the normalisation of x with x_{peak} returned a good collapse of the turbulence intensity's dependence on distance from the grid, such a collapse is not at all evident in Fig. 29 (right). There are many possible causes for this, including lack of sufficient homogeneity, lack of statistical convergence, etc. Further investigations (both wind tunnel measurements and DNS simulations of turbulent flows generated by various fractal grids with various values of N and σ) are now necessary for fully understanding the influence of the number of fractal iterations in the definition of x_{peak}.

4.3 Energy spectra

The production region can be investigated further in terms of frequency power spectra of the streamwise fluctuating velocity at various points in the flow (Fig. 32). These power spectra, obtained on the centreline at six different streamwise locations from $x = 13t_{\min}$ to $78t_{\min}$ (all much smaller than x_{peak}), are calculated using the periodogram technique (see [21] for more details about this technique). Eleven sequences are used here, corresponding to a global time duration equal to $380t_{\min}/U_\infty$ overlapped at 50%, with the use of a Hanning window. The protracted nature of a fractal grid's production region vis a vis that of the regular grid is clear in Fig. 32: the entire energy spectrum jumps up to high values between $x/t_{\min} = 26$ and $x/t_{\min} = 39$ and then subsequently decays in the region $x/t_{\min} \geq 40$. However, the turbulence Reynolds number is not high enough for a Kolmogorov-type $f^{-5/3}$ power-law range

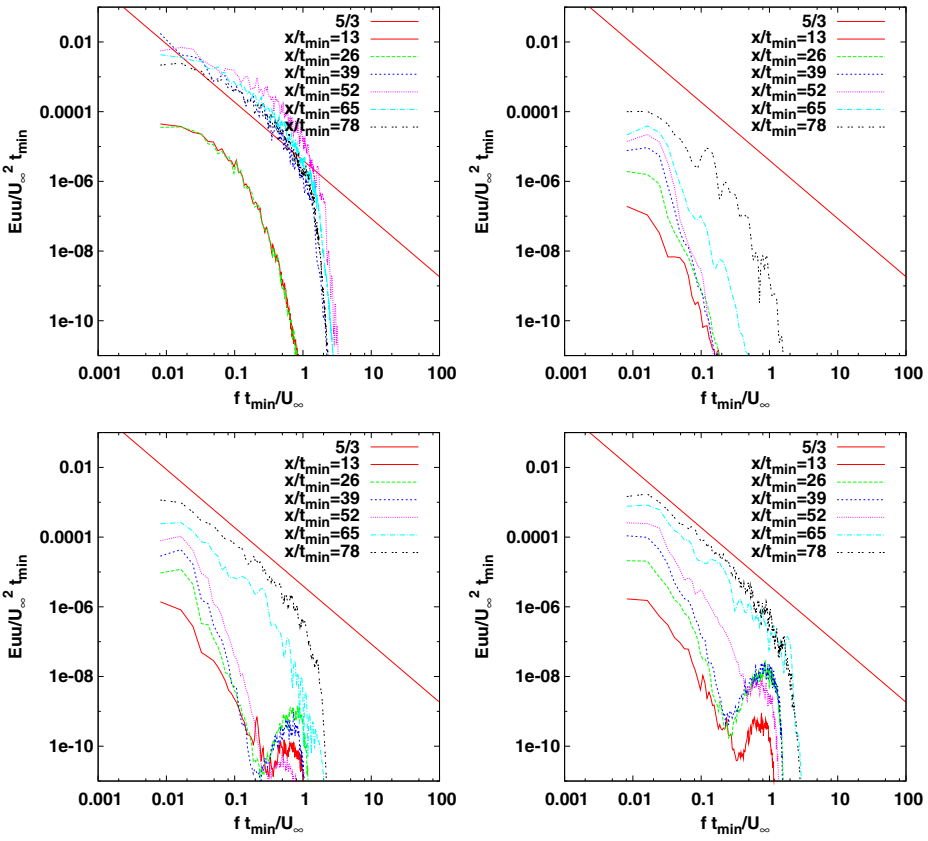

Fig. 32 Power spectra of the streamwise velocity fluctuations in time for six different streamwise locations from $x = 13t_{\min}$ to $78t_{\min}$ on the centreline of the flow. These values of x are all smaller than x_{peak} and therefore in the production region of the flow. The *top left plot* is for the regular grid, the *top right plot* is for the $t_r = 5$ fractal square grid, and the *bottom plots* are for the $t_r = 6.5$ (*left*) and $t_r = 8.5$ (*right*) fractal square grids

anywhere along the centreline. This behaviour is in stark contrast with that observed in the lee of our fractal grids where the energy spectrum continuously increases in magnitude over the range of centreline locations considered. The power spectra in the lee of the $t_r = 6.5$ and $t_r = 8.5$ fractal square grids are perhaps the most interesting: the energy fluctuations amplify at high frequencies near the grid followed by the appearance of lower excited frequencies further downstream from the grid till eventually a broad spectrum is developed with an approximate $f^{-5/3}$ power-law shape in an intermediate range. This $f^{-5/3}$ power-law shape may be present because, compared to the regular grid and the $t_r = 5$ fractal square grid, these two fractal square grids generate the highest turbulence intensities and therefore the highest turbulence Reynolds numbers for a given value of $U_\infty t_{\min}/\nu$. Note also, however, that this $f^{-5/3}$ frequency spectrum appears where the flow is by no means spatially homogeneous and isotropic.

5 Conclusion

Four spatially evolving turbulent flows generated by a regular and three fractal square grids have been investigated by means of DNS. The main results which we have been able to obtain from these simulations are the following:

1. Visualisations suggest that the vorticity field is more intermittent or more clustered when generated by fractal square grids compared to regular grids of same or even lower blockage ratios and at comparable $U_\infty M_{\text{eff}}/\nu$. There is a need to quantify this qualitative observation in the future.
2. Fractal square grids generate protracted regions of higher vorticity and turbulence intensity compared to regular grids of same or even lower blockage ratios and at comparable $U_\infty M_{\text{eff}}/\nu$ (which does not preclue the fact that regular grids actually produce the highest turbulence intensities but only over a short region very close to the grid).
3. We have visualised the multiscale wakes and their interactions in the lee of fractal square grids.
4. We have also calculated various turbulence profiles. The streamwise extent of the present simulations is not long enough and the number of fractal iterations on the grids not large enough for fully homogeneous turbulence to develop. DNS with a longer computational domain in the streamwise direction and with fractal square grids that have $N = 4$ fractal iterations as in the wind tunnel experiments of [4, 14, 22] are now possible with the present fully parallel code [8] on the latest High Performance Computing facilities in Europe. These DNS will be able to provide detailed and accurate comparisons with available wind tunnel data.
5. Our visualisations show that the flow holds clear geometrical imprints of the fractal grids far downstream, a property which could be used in the future for flow design, management and passive control. In particular, in our future simulations, we are going to investigate the different terms of the forcing term f in Eq. 2.
6. Our DNS confirmed the existence of two turbulent regions, one where the turbulence progressively amplifies closer to the grid followed by one where the turbulence decays. The location on the centreline of the peak turbulence value can be evaluated as $x_{\text{peak}} = C(N, \sigma) L_0^2/t_0$. Future DNS with a fractal iteration

number $N = 4$ and new experimental wind tunnel measurements with $N = 3$ will help us to investigate the influence of N on the generated turbulence.

7. One-dimensional energy spectra of fluctuating turbulent velocities at various locations in the production region of the flow reveal how the turbulence is generated at the smallest scales first near the grid where the smallest wakes are dominant, followed by the activation of progressively smaller turbulent frequencies further downstream where progressively larger wakes interact.

Acknowledgements We acknowledge the EPSRC grant EP/G069581 supporting the UK Turbulence consortium for the CPU time made available to us on HECToR without which this study would not have been possible. The authors are grateful to Ning Li for helping with the parallel version of **Incompact3d**. We also thank Eric Lamballais for very useful discussions and acknowledge support from EPSRC Research grants EP/E00847X/1 and EP/F051468/1.

References

1. Bachelor, G.K.: The Theory of Homogeneous Turbulence. Cambridge Univ. Press (1953)
2. Chester, S., Meneveau, C., Parlange, M.B.: Modeling turbulent flow over fractal trees with renormalized numerical simulation. J. Comput. Phys. **225**(1), 427–448 (2007)
3. Coffey, C.J., Hunt, G.R., Seoud, R.E., Vassilicos, J.C.: Mixing effectiveness of fractal grids for inline static mixers. In: Proof of Concept Report for the Attention of Imperial Innovations. http://www3.imperial.ac.uk/tmfc/papers/poc (2007)
4. Hurst, D., Vassilicos, J.C.: Scalings and decay of fractal-generated turbulence. Phys. Fluids **19**, 035103 (2007)
5. Ishihara, T., Gotoh, T., Kaneda, Y.: Study of high Reynolds number isotropic turbulence by direct numerical simulation. Annu. Rev. Fluid Mech. **41**, 165–180, (2009)
6. Laizet, S., Lamballais, E.: High-order compact schemes for incompressible flows: a simple and efficient method with the quasi-spectral accuracy. J. Comput. Phys. **228**(16), 5989–6015 (2009)
7. Laizet, S., Lamballais, E., Vassilicos, J.C.: A numerical strategy to combine high-order schemes, complex geometry and parallel computing for high resolution dns of fractal generated turbulence. Comput. Fluids **39**(3), 471–484 (2010)
8. Laizet, S., Li, N.: Incompact3d, a powerful tool to tackle turbulence problems with up to (10^5) computational cores. Int. J. Numer. Methods Fluids. doi:10.1002/fld.2480 (2011)
9. Laizet, S., Vassilicos, J.C.: Direct numerical simulation of fractal-generated turbulence. In: Proc. DLES-7. Trieste (2008)
10. Laizet, S., Vassilicos, J.C.: Direct numerical simulation of turbulent flows generated by regular and fractal grids using an immersed boundary method. In: Proc. TSFP 6. Seoul (2009)
11. Laizet, S., Vassilicos, J.C.: Multiscale generation of turbulence. J. Multiscale Modelling **1**, 177–196 (2009)
12. Lele, S.K.: Compact finite difference schemes with spectral-like resolution. J. Comput. Phys. **103**, 16–42 (1992)
13. Lorenz, E.N.: The interaction between a mean flow and random disturbances. Tellus **5**(3), 238–250 (1953)
14. Mazellier, N., Vassilicos, J.C.: Turbulence without Richardson–Kolmogorov cascade. Phys. Fluids **22**, 075101 (2010)
15. Mazzi, B., Vassilicos, J.C.: Fractal-generated turbulence. J. Fluid Mech. **502**, 65–87 (2004)
16. Mohamed, M.S., LaRue, J.C.: The decay power law in grid-generated turbulence. J. Fluid Mech. **219**, 195–214 (1990)
17. Nagata, K., Suzuki, H., Sakai, H., Hayase, Y., Kubo, T.: Direct numerical simulation of turbulence characteristics generated by fractal grids. Int. Rev. Phys. **5**, 400–409 (2008)
18. Nagata, K., Suzuki, H., Sakai, H., Hayase, Y., Kubo, T.: Direct numerical simulation of turbulent mixing in grid-generated turbulence. Phys. Scr. **132**, 014054 (2008)
19. Parnaudeau, P., Carlier, J., Heitz, D., Lamballais, E.: Experimental and numerical studies of the flow over a circular cylinder at Reynolds number 3,900. Phys. Fluids **20**, 085101 (2008)

20. Parnaudeau, P., Lamballais, E., Heitz, D., Silvestrini, J.H.: Combination of the immersed boundary method with compact schemes for DNS of flows in complex geometry. In: Proc. DLES-5. Munich (2003)
21. Press, W.H., Teukolsky, S.A., Vetterling, W.T., Flannery, B.P.: Numerical Recipes. Cambridge University Press, Cambridge (1992)
22. Seoud, R.E., Vassilicos, J.C.: Dissipation and decay of fractal-generated turbulence. Phys. Fluids **19**, 105108 (2007)
23. Stresing, R., Peinke, J., Seoud, R.E., Vassilicos, J.C.: Defining a new class of turbulent flows. Phys. Rev. Lett. **104**(19), 194501 (2010)
24. Townsend, A.A.: The Structure of Turbulent Shear Flows. Cambridge Univ. Press (1956)